REPORT DOCUMENTATION PAGE

Form Approved OMB NO. 0704-0188

1. REPORT DATE (DD-MM-YYYY)	2. REPORT TYPE	3. DATES COVERED (From - To)
10-10-2014	Final Report	15-May-2009 - 14-Jan-2013

4. TITLE AND SUBTITLE

Final Report: Uncooled Infrared Microbolometers and Silicon Germanium Oxide (SixGe1-xOy) Infrared Sensitive Material for Long Wavelength Detection

5a. CONTRACT NUMBER

W911NF-09-1-0158

5b. GRANT NUMBER

5c. PROGRAM ELEMENT NUMBER

611102

6. AUTHORS

M. Almasri, M. L. Hai, M. Hesan, Q. Cheng, M. Jalal, A. J. Syllaios, and S. Ajmera

5d. PROJECT NUMBER

5e. TASK NUMBER

5f. WORK UNIT NUMBER

7. PERFORMING ORGANIZATION NAMES AND ADDRESSES

University of Missouri - Columbia
310 Jesse Hall

Columbia, MO   65211 -1230

8. PERFORMING ORGANIZATION REPORT NUMBER

9. SPONSORING/MONITORING AGENCY NAME(S) AND ADDRESS (ES)

U.S. Army Research Office
P.O. Box 12211
Research Triangle Park, NC 27709-2211

10. SPONSOR/MONITOR'S ACRONYM(S)

ARO

11. SPONSOR/MONITOR'S REPORT NUMBER(S)

55969-EL.3

12. DISTRIBUTION AVAILIBILITY STATEMENT

Approved for Public Release; Distribution Unlimited

13. SUPPLEMENTARY NOTES

The views, opinions and/or findings contained in this report are those of the author(s) and should not contrued as an official Department of the Army position, policy or decision, unless so designated by other documentation.

14. ABSTRACT

This report presents a detailed characterization of infrared sensitive silicon germanium oxide (SixGeyO1-x-y) thin films. The results demonstrated that a high TCR and a low corresponding resistivity can be achieved using various compositions, for example, $Si_{0.054}Ge_{0.877}O_{0.069}$ film has achieved a TCR and a resistivity of $-3.516/K$, and 629 ohm-cm, respectively. The lowest measured resistivity and the corresponding TCR were 90.73 ohm-cm and -1.653 %/K respectively, using $Si_{0.206}Ge_{0.650}O_{0.144}$ for film deposited at room temperature, whereas the highest achieved TCR and the corresponding resistivity at room temperature were 5.017 %/K, and 39.1×10^3 ohm-cm

15. SUBJECT TERMS

Silicon germanium oxide, SiGeO, uncooled microbolometer, Infrared material, infrared detector, noise

16. SECURITY CLASSIFICATION OF:			17. LIMITATION OF ABSTRACT	15. NUMBER OF PAGES	19a. NAME OF RESPONSIBLE PERSON
a. REPORT	b. ABSTRACT	c. THIS PAGE			Mahmoud Almasri
UU	UU	UU	UU		

19b. TELEPHONE NUMBER

573-882-0813

Report Title

Final Report: Uncooled Infrared Microbolometers and Silicon Germanium Oxide (SixGe1-xOy) Infrared Sensitive Material for Long Wavelength Detection

ABSTRACT

This report presents a detailed characterization of infrared sensitive silicon germanium oxide (SixGeyO1-x-y) thin films. The results demonstrated that a high TCR and a low corresponding resistivity can be achieved using various compositions, for example, Si0.054Ge0.877O0.069 film has achieved a TCR and a resistivity of –3.516/K, and 629 ohm-cm, respectively. The lowest measured resistivity and the corresponding TCR were 90.73 ohm-cm and –1.653 %/K respectively, using Si0.206Ge0.650O0.144 for film deposited at room temperature, whereas the highest achieved TCR and the corresponding resistivity at room temperature were -5.017 %/K, and 39.1×103 ohm-cm, respectively, using Si0.167Ge0.762O0.071 for films deposited at room temperature. The X-ray diffraction study demonstrated that the films are amorphous. The peak broadening and peak shift was used to explain the dependence of TCR and resistivity on varying silicon at fixed oxygen concentration, and varying oxygen at fixed Si concentration. Raman spectroscopy results are used relate the TCR and resistivity of Si-Ge-O films with the Ge-Si, and Ge-Ge chemical bonding. The spectra showed dependence on varying silicon at fixed oxygen or at fixed Si. Uncooled microbolometers were fabricated with various Si-Ge-O compositions. Voltage noise PSD was measured and optimized, using annealing in vacuum at 200 oC, 250 oC, and 300 oC.

Enter List of papers submitted or published that acknowledge ARO support from the start of the project to the date of this printing. List the papers, including journal references, in the following categories:

(a) Papers published in peer-reviewed journals (N/A for none)

<u>Received</u>   <u>Paper</u>

TOTAL:

Number of Papers published in peer-reviewed journals:

(b) Papers published in non-peer-reviewed journals (N/A for none)

<u>Received</u>   <u>Paper</u>

TOTAL:

Number of Papers published in non peer-reviewed journals:

<div align="center">

(c) Presentations

</div>

1. M. L. Hai, M. Hesan, J. Lin, A. J. Syllaios, S. Ajmera and M. Almasri, "Amorphous (SixGeyO1-x-y) Thin Film for Uncooled Infrared Microbolometers," To be submitted to IEEE Electron Devices. The paper is written and will be submitted to L-3 Communications for review before submission to the journal.

2. M. Jalal, M. L. Hai, A. J. Syllaios, S. Ajmera and M. Almasri, "Noise Optimization of Amorphous SixGeyO1-x-y Thin Films,". To be submitted to Thin Solid Films. The paper is written and submitted to L-3 Communications for review before submission to the journal.

3. Qi Cheng, R. Anvari, Q. Cheng, M. Hai, T. Bui, A. J. Syllaios, S. Ajmera, M. Almasri*, "Silicon Germanium Oxide (SixGe1-xOy) for Uncooled Infrared Microbolometer," MRS, vol. 1245, pp 1245-A18-04, 2010.

4. M. L. Hai, M. Hesan, J. Lin, Q. Cheng, M. Jalal, A. J. Syllaios, S. Ajmera and M. Almasri, Uncooled silicon germanium oxide (SixGeyO1-x-y) thin films for infrared detection", Proc. SPIE 8353, 835317, 2012.

Number of Presentations: 4.00

<div align="center">

Non Peer-Reviewed Conference Proceeding publications (other than abstracts):

</div>

<u>Received</u>   <u>Paper</u>

    TOTAL:

Number of Non Peer-Reviewed Conference Proceeding publications (other than abstracts):

<div align="center">

Peer-Reviewed Conference Proceeding publications (other than abstracts):

</div>

<u>Received</u>   <u>Paper</u>

08/31/2012   1.00   S. Ajmera, M. Almasri, A. J. Syllaios, M. L. Hai, M. Hesan, J. Lin, Q. Cheng, M. Jalal. Uncooled silicon germanium oxide (Si,
                    Infrared Technology and Applications XXXVIII. 23-APR-12, Baltimore, Maryland, USA. : ,

08/31/2012   2.00   Reza Anvari, Qi Cheng, Muhammad Lutful Hai, Truc Phan Bui, A. J. Syllaios, S. K. Ajmera, Mahmoud F. Almasri. Silicon Germanium Oxide (SixGeyO1-x-y) Infrared Sensitive Material for Uncooled Detectors, MRS Spring Meeting 2010. 05-APR-10, . : ,

    TOTAL: **2**

Number of Peer-Reviewed Conference Proceeding publications (other than abstracts):

(d) Manuscripts

Received   Paper

    TOTAL:

Number of Manuscripts:

Books

Received   Book

    TOTAL:

Received   Book Chapter

    TOTAL:

Patents Submitted

Patents Awarded

Awards

Graduate Students

NAME	PERCENT SUPPORTED	Discipline
Muhammad Hai	1.00	
Md Jalal	0.25	
Feng, Feng	0.25	
FTE Equivalent:	**1.50**	
Total Number:	**3**	

Names of Post Doctorates

NAME	PERCENT SUPPORTED
FTE Equivalent:	
Total Number:	

Names of Faculty Supported

NAME	PERCENT SUPPORTED	National Academy Member
Mahmoud Almasri	0.10	
FTE Equivalent:	**0.10**	
Total Number:	**1**	

Names of Under Graduate students supported

NAME	PERCENT SUPPORTED	Discipline
Muhmmad Hesan	0.10	
FTE Equivalent:	**0.10**	
Total Number:	**1**	

Student Metrics
This section only applies to graduating undergraduates supported by this agreement in this reporting period

The number of undergraduates funded by this agreement who graduated during this period: 1.00

The number of undergraduates funded by this agreement who graduated during this period with a degree in science, mathematics, engineering, or technology fields:...... 1.00

The number of undergraduates funded by your agreement who graduated during this period and will continue to pursue a graduate or Ph.D. degree in science, mathematics, engineering, or technology fields:...... 0.00

Number of graduating undergraduates who achieved a 3.5 GPA to 4.0 (4.0 max scale):...... 0.00

Number of graduating undergraduates funded by a DoD funded Center of Excellence grant for Education, Research and Engineering:...... 0.00

The number of undergraduates funded by your agreement who graduated during this period and intend to work for the Department of Defense 0.00

The number of undergraduates funded by your agreement who graduated during this period and will receive scholarships or fellowships for further studies in science, mathematics, engineering or technology fields:...... 0.00

Names of Personnel receiving masters degrees

NAME
Md Jalal
Total Number: **1**

Names of personnel receiving PHDs

NAME

Total Number:

Names of other research staff

NAME   PERCENT SUPPORTED

FTE Equivalent:
Total Number:

Sub Contractors (DD882)

Inventions (DD882)

Scientific Progress

See attached file

Technology Transfer

Final Report

Uncooled Infrared Microbolometers and Silicon Germanium Oxide (Si$_x$Ge$_{1-x}$O$_y$) Infrared Sensitive Material for Long Wavelength Detection

The fourth year of the project was mainly focused on the following:

A. Deposition of silicon-germanium-oxide (Si$_x$Ge$_y$O$_{1-x-y}$) and determining the element's composition,
B. TCR and Resistivity measurement
C. X-ray diffractions (XRD), Raman spectroscopy and FTIR of the thin films
D. Infrared detector design, fabrication with and without the air gap
E. Noise measurement of the fabricated infrared detectors and improvement of noise PSD by annealing.
F. PhD and MS Thesis.

Publications

1. Qi Cheng, R. Anvari, Q. Cheng, M. Hai, T. Bui, A. J. Syllaios, S. Ajmera, M. Almasri*, "Silicon Germanium Oxide (Si$_x$Ge$_{1-x}$O$_y$) for Uncooled Infrared Microbolometer," *MRS*, vol. 1245, pp 1245-A18-04, 2010.
2. M. L. Hai, M. Hesan, J. Lin, Q. Cheng, M. Jalal, A. J. Syllaios, S. Ajmera and M. Almasri, Uncooled silicon germanium oxide (Si$_x$Ge$_y$O$_{1-x-y}$) thin films for infrared detection", Proc. SPIE 8353, 835317, 2012.
3. M. L. Hai, M. Hesan, J. Lin, A. J. Syllaios, S. Ajmera and M. Almasri, "Amorphous (Si$_x$Ge$_y$O$_{1-x-y}$) Thin Film for Uncooled Infrared Microbolometers," In final writing stage. To be submitted to IEEE Electron Devices.
4. M. Jalal, M. L. Hai, A. J. Syllaios, S. Ajmera and M. Almasri, "Noise Optimization of Amorphous Si$_x$Ge$_y$O$_{1-x-y}$ Thin Films by Si$_3$N$_4$ Passivation and Annealing in Vacuum," In final writing stage. To be submitted to Thin Solid Films.

INTRODUCTION AND BACKGROUND

Infrared (IR) imaging cameras have a broad spectrum of commercial and military applications including surveillance, threat detection, target recognition, medical diagnostics, firefighting, surveillance and security [1, 2]. These cameras are developed by companies such as L-3 Communication[3-8], Raytheon[9-11], DRS[12-15], BAE Systems[16-19], Lockheed Martin[20], Honeywell[21], CEA-LETI and ULIS[22-28], INO[29, 30], Infrared Vision Technology Corporation[31, 32] and SCD Semi-Conductor Devices Ltd[33] They are mainly based on Vanadium Oxide (VO$_x$)[2, 18, 34] or amorphous silicon (*a*: Si) technology[3, 7, 8, 11, 26, 27]. Several other IR sensitive materials have been used in uncooled Yttrium-Barium-Copper-Oxide (YBaCuO)[35-37], Silicon Germanium (SiGe)[23, 38], Silicon Germanium Oxide (Si-Ge-O) [39-46], metals[47, 48] and *poly*:SiGe[49-51] (See Table 1).

Vanadium Oxide (VOx) and amorphous silicon (*a*:Si) technology are the mainstream materials and have comparable performance. These materials have been used for full production of cutting edge cameras for many years[5, 10, 12, 16]. VOx has an acceptable TCR between 2 %/K to 2.4 %/K[10, 52] and a relatively low 1/*f* noise of 2.339×10^{-8} V/Hz$^{1/2}$ at 5 Hz with a bias of 19.3 μA[53]. The fabricated VOx microbolometers with a size of 25×25 μm^2 by the Raytheon group have achieved responsivity, thermal time constant and noise equivalent temperature difference (NETD) of 2.5×10^7 V/W, 3-15 ms, and less than 50 mK, respectively [9, 10, 54]. While VOx technology is ground breaking, it is encumbered by many factors limiting its ability to leverage its greater sensitivity. These factors include a complicated design and spatial

noise[55] and VOx is difficult to fabricate within the requirements of readout circuitry. The result is less expensive, rather than inexpensive IR technology. *a*:Si has achieved wide range of TCR with high values between 2.5 %/K and 5 %/K with a corresponding resistivity range from 200 Ω-cm to 1×10^5 Ω-cm[8]. When the TCR was increased to 3.9 %/K, the 1/*f*-noise was not increased. This TCR value was used to build fully operable 17×17 µm^2 LWIR focal plane array[7, 8]. In addition, the fabricated *a*:Si microbolometers with a size of 17×17 µm^2 by L-3 Communications' group have achieved NETD less than 50 mK for spectral window between 8-12 µm, thermal time constant ~10 ms using *a*:Si material with TCR ~3.2 %/K[7]. It is noted that *a*:Si microbolometers took advantages of the extensive knowledge available in Si manufacturing processes, and the extensive research in Si-based solar cells and flat panel displays. Thus, the overall production cost of *a*:Si based cameras is low, and the yield is high which has enabled high volume commercial market[5]. Many other infrared materials have been used in uncooled microbolometers. Amorphous silicon (*a*:Si) has a TCR between –2 %/K and –3.9 %/K with a marginal 1/*f* noise[11, 26, 27]. YBaCuO films achieve TCR between 3-3.5%/K and 1/*f* noise of 4×10^{-14} V^2/Hz at 7 Hz with 0.41 µA, but this material is not conventionally used in semiconductor processing[35, 37]. The resistivity of SiGe can be kept low by controlling the doping level, but this sets an upper limit to TCR (–2.5 –3%/K). Processing of *poly*:SiGe materials to achieve the desired crystallinity requires temperatures as high as 650 °C[38]. Metals have very low 1/*f* noise, and low resistivity. However, the low TCR value resulted in low performance in terms of responsivity and detectivity [48]. *poly*:Si has a TCR of 2%/K[49]. Germanium (Ge) has a lower 1/*f* noise than Silicon devices but its TCR is only 1%/K. We have selected to investigate amorphous $Si_xGe_yO_{1-x-y}$ for the IR sensing layer as a new addition to the mainstream materials because of its excellent IR radiation absorption, and mechanical and electrical properties at room temperature. It can achieve high TCR with a low resistivity and acceptable 1/*f* noise. Thus, the device performance (responsivity and detectivity) can be improved without increasing the 1/*f*-noise. A summary of TCR of various IR materials are shown in Table 1.

Table 1. Temperature coefficient of resistance (TCR) of common uncooled infrared materials

Infrared Materials	TCR (%/K)	References
VOx	2 - 2.4	[10, 52]
a:Si	2 - 3.9	[3, 4, 8, 56-60]
YBaCuO	2.88 – 3.5	[35, 37]
Si-Ge	2 – 3	[49, 61]
Si-Ge-O	See Table 2	[40-46, 62]
Metal	0.2	[48, 63, 64]
Poly: Si	2	[65]
Ge	1	[56]

Several research groups have studied Si-Ge-O compound as an IR sensitive material (See Table 2). Ahmed *et al* [44] determined that for a fixed O_2 concentration, the TCR, and resistivity increases as Si concentration increases up to 5-10 atomic % and then starts to decrease. They also found out that they are proportional to the O_2 concentration in $Si_xGe_{1-x}O_y$ films. The use of high O_2 concentration (14% and above) might have resulted in high resistivity and TCR. It is noted that they have used very few data point to describe the behavior of the film. A high TCR value of –4.88%/K was reported but with a high resistivity of 38 kΩ-cm for $Si_xGe_{1-x}O_y$ with 2.5 atomic % of Si and 18.8 atomic % of O_2. Clement *et al.* sputtered $Ge_{0.85}Si_{0.15}$ compound target in argon/oxygen environment[45]. They have measured under optimum conditions, a resistivity and a corresponding TCR of 10 kΩ-cm and 5%/K, respectively. A similar deposition method was performed by Rana *et al* [46]. In earlier work, they fixed a piece of silicon

(cut from silicon wafer) to a Ge target and deposited using one power source, in later work they deposit $Si_{0.15}Ge_{0.85}$ from one target in argon/oxygen environment [66]. Their findings agreed with Ahmed *et al.* However, this study used a specific film concentration $Si_{0.15}Ge_{0.85}O_y$ while the O_2 was varied between 0 - 9%.

Table 2. This table report the most recent results of TCR and resistivity of Si-Ge-O.

TCR (%/K)	Resistivity (Ω-cm)	References
− (2.27 - 8.69)	4.22×10^2 - 3.47×10^9	[43, 46]
−5	10^4	[45]
−5	3.8×10^4	[42, 44]
−6.43	3.34×10^2	[39-41] Our group

This work utilizes amorphous $Si_xGe_yO_{1-x-y}$ as the IR sensing layer for the fabrication of uncooled microbolometers because of its excellent IR radiation absorption, and mechanical and electrical properties at room temperature. Si and Ge based compounds are standard materials in silicon integrated circuits providing a wide range of established knowledge for application to the fabrication of the microbolometer array. The activation energy, electrical resistivity and TCR of $Si_xGe_yO_{1-x-y}$ primarily depend upon the oxygen content in the film, which is controlled during sputter deposition. At a specific silicon, and oxygen percentage, a high TCR and low resistivity values can be achieved. A compromise between resistance and TCR is required, as the microbolometer focal plane array (FPA) is connected to readout electronics that require resistance below 100 kΩ. This resistivity value is compatible with conventional readout integrated circuitry. Finally, it is compatible with CMOS technology due to the low deposition temperature and the use of conventional dry-etch processing. Therefore, the FPA can be easily integrated with the readout electronics[42, 45].

We report the results of TCR and resistivity as a function of temperature of the deposited $Si_xGe_yO_{1-x-y}$. The influence of changing silicon and oxygen contents on TCR, resistivity is discussed, mainly for a low level of O_2 concentration. The amorphous behaviors of the films were studied as a function of fixed oxygen while varying Si using X-Ray diffraction. The status of oxygen bonding to both silicon and germanium were investigated using Fourier Transform Infrared (FTIR) and Raman spectroscopy. The Ge-O bonds are controlled to achieve the desired resistivity and TCR values by varying the silicon content. The atomic composition of Si, Ge, and oxygen in the deposited thin films were determined and analyzed using energy dispersive X-ray spectroscopy (EDX). We will also report the fabrication of uncooled microbolometers with and without an air gap with different $Si_xGe_yO_{1-x-y}$ compositions for the purpose of measuring and optimizing the noise in these films. In addition, we are reporting the reduction of the voltage noise power spectral density (PSD) of uncooled $Si_xGe_yO_{1-x-y}$ microbolometers by passivating the devices with Si_3N_4 layers and annealing them at 200 °C, 250 °C, or 300 °C in vacuum at different time interval. Four set of devices with different Si-Ge-O element compositions were studied in details. The voltage noise power spectral densities were analyzed and Hooge's parameters were determined.

UNCOOLED MICROBOLOMETER

A thermal detector exhibits a change in electrical property that accompanies a change in temperature of the sensitive element caused by absorption of IR radiation. A microbolometer is a thermal sensor that exhibits a change in resistance with respect to a change of temperature of the sensing material accompanying the absorption of IR radiation. It consists of a thin microbridge suspended above a silicon substrate. The bridge is supported by two narrow arms, which serve as support structure, conductive legs

and thermal isolation legs. Encapsulated in the center of the bridge is a thin layer of IR sensitive material[35, 57]. The performance of the microbolometer can be significantly enhanced at specific spectral wavelength windows if the IR sensing material achieves a high TCR with a relatively low resistivity and low voltage noise. The TCR shows how rapidly the resistance of a material responds to a change in temperature. It is given by:

$$TCR = \frac{1}{R}\frac{dR}{dT} = \frac{1}{R}\frac{\Delta R}{\Delta T} = -\frac{E_a}{kT^2} \tag{1}$$

$$R(T) = R_0 \exp\left(\frac{E_a}{kT}\right) \tag{2}$$

where E_a is the activation energy, k is the Boltzmann constant, $R(T)$ is the resistance at temperature T, R_0 is the initial resistance. A four point probe method was used to characterize the TCR and resistivity of the deposited thin films and devices. The relation between the measured resistance and the calculated resistivity of $Si_xGe_yO_{1-x-y}$ films can be expressed by the following two equations:

$$R = \int_s^{2s} \frac{\rho}{2\pi t}\frac{dx}{x} = \frac{\rho}{2\pi t}\ln 2 = \frac{V}{I} \tag{3}$$

$$\rho = \frac{\pi t}{\ln 2}\left(\frac{V}{I}\right) \tag{4}$$

where R is the resistance of the film, ρ is the sheet resistivity, t is the thickness of the thin film, V and I are the measured voltage and current respectively.

The performance of the microbolometers can be improved substantially and reach the temperature fluctuation noise performance if noise is eliminated or reduced. The reduction of noise is crucial to the next generation of uncooled thermal cameras since it will allow the detector to reach the background limited noise performance and further improve the noise equivalent temperature difference (NETD). This will include the noise generated by the IR sensing element (Johnson noise, random telegraph switching (RTS) and 1/f flicker noise), temperature fluctuation noise, and background voltage noise. Johnson noise, ΔV_J, is due to the thermal agitation of charge carriers. It is inherent in the detecting element and cannot be avoided. RTS is caused by unknown imperfections in material structure and contacts, and is therefore most often observed in very small devices, or very high resistivity materials such as the one studied in this work. 1/f-noise is observed at low frequencies, usually due to the fluctuations in both carrier concentration and carrier mobilities, arising from carrier trapping and detrapping mechanisms and surface state scattering. It also depends on the deposition techniques, material, dimensions and electrical contacts [57, 67, 68]. Another aspect of 1/f-noise is its volume dependency. Thus, increasing the thickness of the IR sensitive film will reduce the noise level significantly. However, this will result in large thermal mass and hence low responsivity and detectivity and large thermal time constant[69]. The electrical noise increases at lower frequencies is due to the increasing contribution of 1/f-noise[49]. The 1/f noise can be expressed by Hooge's formula:

$$S_V = \frac{K_f V_{dc}^{\beta}}{f^{\gamma}} \tag{5}$$

$$K_f = \frac{\alpha_H}{N} \tag{6}$$

where S_V is the noise voltage PSD, f' is the electrical frequency with γ close to 1 for 1/f noise[38], K_f is the 1/f-noise coefficient (flicker noise coefficient). It is given by equation 6 where α_H is Hooge's constant

that gives the magnitude of *1/f* noise, *N* is the number of fluctuators in the sample and is volume dependent. Therefore, K_f is related to the volume normalized inherent noise. It depends on the quality of the crystal, and on the scattering mechanisms that determine the mobility, μ [71]. V_{dc} is the DC bias voltage equals $I_B \times R$ where the value of β is 2. The values of γ, β, and K_f were determined by taking the logarithm of equation 2:

$$\log_{10} S_V = \beta \log_{10} V_{DC} - \gamma \log_{10} f + \log_{10} K_f$$

(4)

This is basically a straight line equation of $\log_{10} S_V$ versus $\log_{10} V_{DC}$ where β is the slope, and the last two terms of equation 4 are constant for a specific frequency. Thus, the value of β can be determined from the average slope of $\log_{10}(S_V)$ versus $\log_{10}(I_b)$ plot using 1, 5 and 10 Hz at different level of applied bias current (80 nA, 300 nA and 650 nA). Similarly, the value γ can be determined from the average slope of $\log_{10}(S_V)$ versus $\log_{10}(f)$ plot at the same constant currents in the frequency range 1-10 Hz. The average value of K_f can be determined by substituting the calculated value of γ and β for each bias current into equation 3 at 10 Hz.

Deposition of Si$_x$Ge$_y$O$_{1-x-y}$ and determining the element's composition

Si$_x$Ge$_y$O$_{1-x-y}$ thin films were grown by RF magnetron sputtering, by co-depositing Si and Ge thin film simultaneously from two deposition targets in an oxygen and argon environment on a p-type silicon substrate, an oxidized silicon substrate (with 0.6 μm oxide layer), and on a glass slide. The depositions were performed at room temperature at 4 mTorr. The targets were 3" undoped 99.999% pure silicon and n-type germanium. Prior to deposition, the substrates were cleaned with pirhana solution, and the sputtering chamber was evacuated to a base pressure between 0.5-3 μTorr. The elemental concentrations of Si and Ge were varied by adjusting RF power applied to the silicon and germanium target and by varying the oxygen flow of the gas mixture in the deposition chamber.

The thin films that were deposited directly on silicon substrates were used to determine the element's concentrations using Energy-dispersive X-ray spectroscopy (EDX). They were measured by energy-dispersive X-ray analysis in a FEI Quanta 600 FEG scanning electron microscope. An accelerating voltage of 4 keV and 120s scanning period were applied to create scanning element spectrum. Standard peaks of Ge, Si and O as well as the atomic concentration in the samples were determined from this experiment. A typical EDX spectrum of Si$_x$Ge$_y$O$_{1-x-y}$ is shown in Figure 1. The total thickness of Si-Ge-O with different compositions was fixed to approximately 300 nm. This was achieved by fixing the deposition power and adjusting the deposition time between samples with different compositions. The thickness of the thin film was measured using KLA-Tencor profiler (P16+).
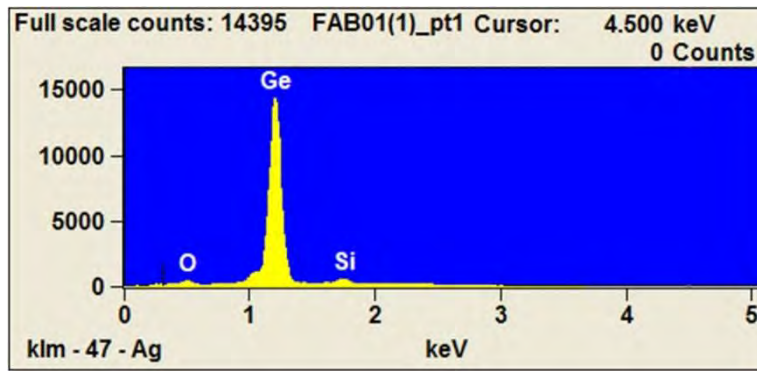
Figure 1: Element composition of $Si_{0.053}Ge_{0.875}O_{0.072}$.

TCR and Resistivity experimental setup

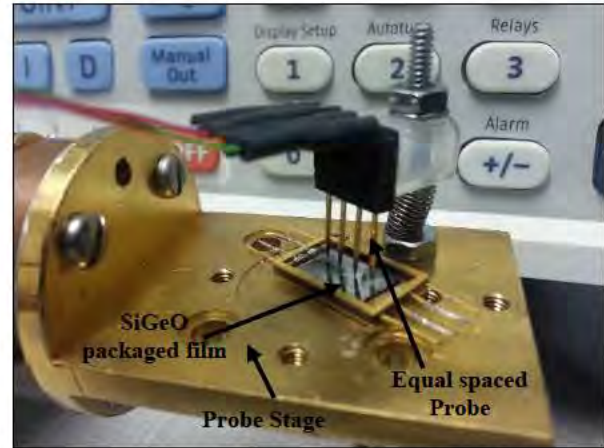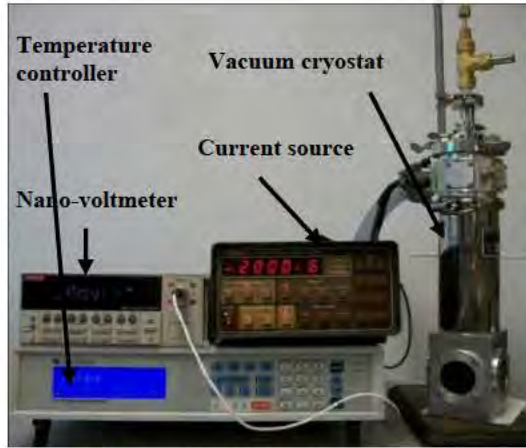**Figure 2:** Experimental set up for the measurement of resistance vs. temperature characteristics. An image of a) the whole setup, b) $Si_xGe_yO_{1-x-y}$ packaged sample mounted on the base stage of equally spaced 4-probe sample holder inside a closed-cycle cryostat.

The TCRs and resistivities of $Si_xGe_yO_{1-x-y}$ thin films were measured using the oxidized silicon substrates ($Si/SiO_2/Si_xGe_yO_{1-x-y}$). First, the wafer was diced into small dies with an area of approximately 1×0.5 cm^2 and then mounted in a ceramic flat pack package by a heat conductive epoxy. The package was heated at 55 °C for 15 min to cure the epoxy. The sample was then mounted firmly on the base stage of a special 4-probe sample holder inside a closed-cycle cryostat (Janis VPF-100 cryostat). The resistance

versus temperature (R-T) characteristics, electrical resistivity and the corresponding temperature coefficient of resistance (TCR) measurements were performed using 4 point probe technique. A programmable current source (Keithley Model 220) is used to apply a fixed current and high precision voltmeter (Keithley model 2182 nano-voltmeter) is used to measure the voltage across the two inner probes. The temperature was varied from 0 °C to 70 °C with 1-2 °C intervals, and controlled by a temperature controller (Lakeshore 336 temperature controller). At each temperature set-point 150 data points were collected and averaged to measure the R-T behavior. The experimental setup for R-T measurement is shown in Figure 2.

TCR and resistivity measurement results

The activation energy (E_a) was used to study the effects of silicon and oxygen on the electrical properties of $Si_xGe_yO_{1-x-y}$ thin film. The E_a was calculated from the slope of Arrhenius plot of resistance versus $1/kT$ as shown in Figure 3(a,c). The solid line in the figure is the measured data and the gray shaded line is the corresponding linear fitting of that curve. Both the measured and fitted curve resembles each other very closely, which is a good indication of the measurement accuracy. The resistance versus temperature (R-T) characteristics, electrical resistivity and the corresponding TCR were plotted in Figure 3. The TCR denoted by "Measured", was plotted from the measured data directly. The TCR denoted by "Calculated", was determined and plotted using Equation 4 where the E_a was deduced from the slope of Arrhenius plot. This figure include a film with a relatively high TCR along with a low resistivity value at room temperature of –3.516/K, and 629 Ω-cm, respectively, using $Si_{0.054}Ge_{0.877}O_{0.069}$, and the highest achieved

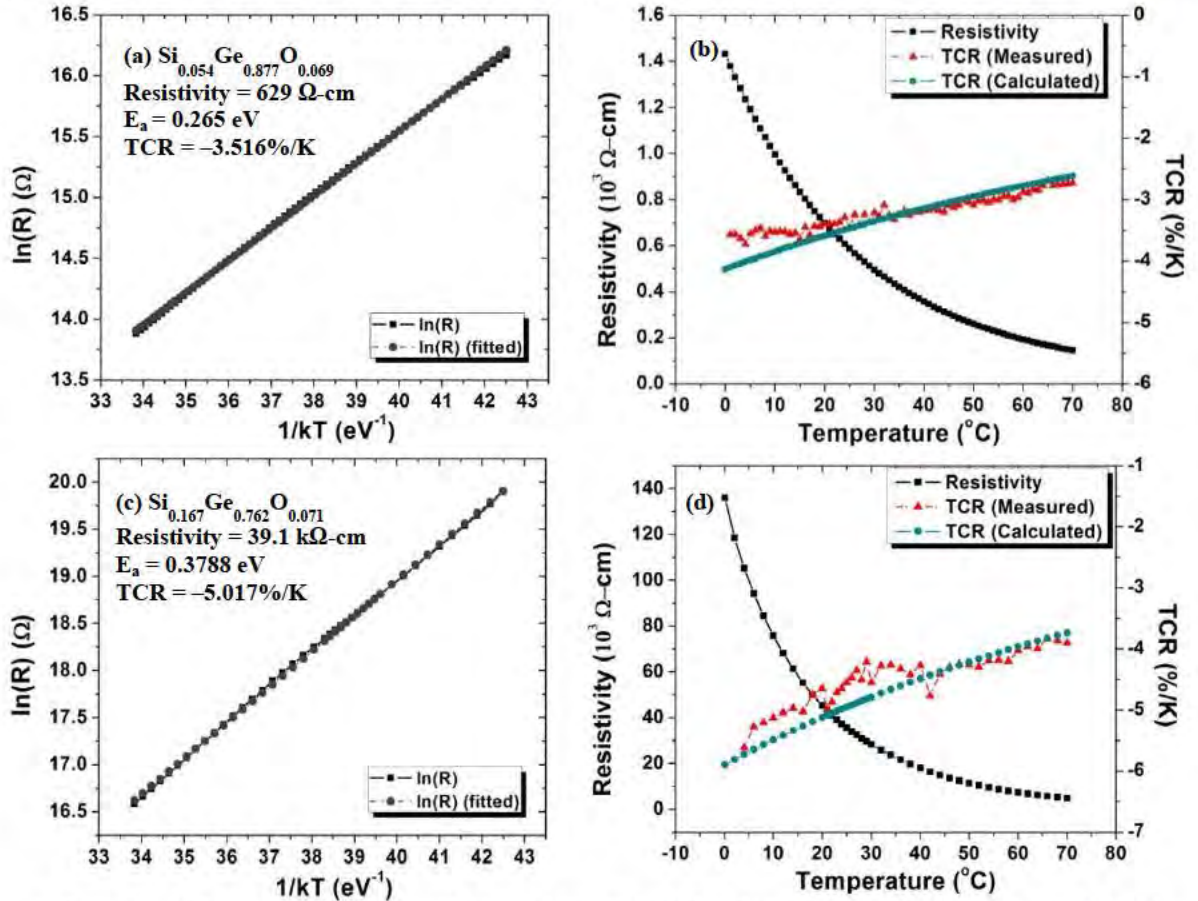**Figure 3:** Arrhenius plot of resistance versus $1/kT$, and TCR and resistivity versus temperature of (a, b) $Si_{0.054}Ge_{0.877}O_{0.069}$, (c, d) $Si_{0.167}Ge_{0.762}O_{0.071}$ films deposited at room temperature.

TCR along with the corresponding resistivity at room temperature were –5.017 %/K and 3.91×10^4 Ω-cm, respectively using $Si_{0.167}Ge_{0.760}O_{0.071}$ for films deposited at room temperature, whereas, the lowest achieved measured resistivity and the corresponding TCR were 119.6 Ω-cm and –2.202 %/K, respectively, using of $Si_{0.135}Ge_{0.838}O_{0.027}$. It is noted that the R-T behavior is exponential and following the relation in equation 2.

The TCR was plotted as a function of resistivity for over 340 films with different Si, Ge, and O_2 compositions in Figure 4. The measured TCR and resistivity for all films regardless of the element's concentrations were also plotted as a function of Si concentration in Figure 5a, and as a function of O_2 concentration in Figure 5b. The results clearly show that there are several films with specific compositions achieve a relatively high TCR above –3.75%/K with a corresponding resistivity values below 1.0 kΩ-cm, which is acceptable for the readout electronics. The rest of the films have high resistivity values. The film with highest TCR has a very high resistivity and thus is not useful for IR imaging.

In order to assess how the element concentrations dictates the electrical behavior, the trend of TCR values were plotted against the Si concentration (see Figure 5a and 5c) and O_2 concentration (see Figure 5b and 5d) using polynomial fitting. The error bars in Figure 5c and 5d indicates the variation due to changes in composition of other constituent material, for a fixed concentration of material of concern. More objectively if we look in to Figure 5c, it is observed that the TCR increases as O_2 concentration increases from very low (~1%) to moderate (~10%) and shows more stable behavior afterwards. Whereas for Si concentration at lower level we observe a similar pattern in increasing TCR from ~2% to ~8% and starts decreasing as Si concentration increase up to ~30%, after which the behavior appears to be more stable.

Moreover it is clearly visible that the error bars more widely spread in Figure 5d than that of Figure 5c, that indicates that for a fixed O_2 concentration there is less impact of changes in Si concentration. But for a fixed Si concentration changes in O_2 concentration changes the TCR more. In essence it can be concluded that atomic concentration of oxygen prevails in the TCR much more than of silicon7 concentration.
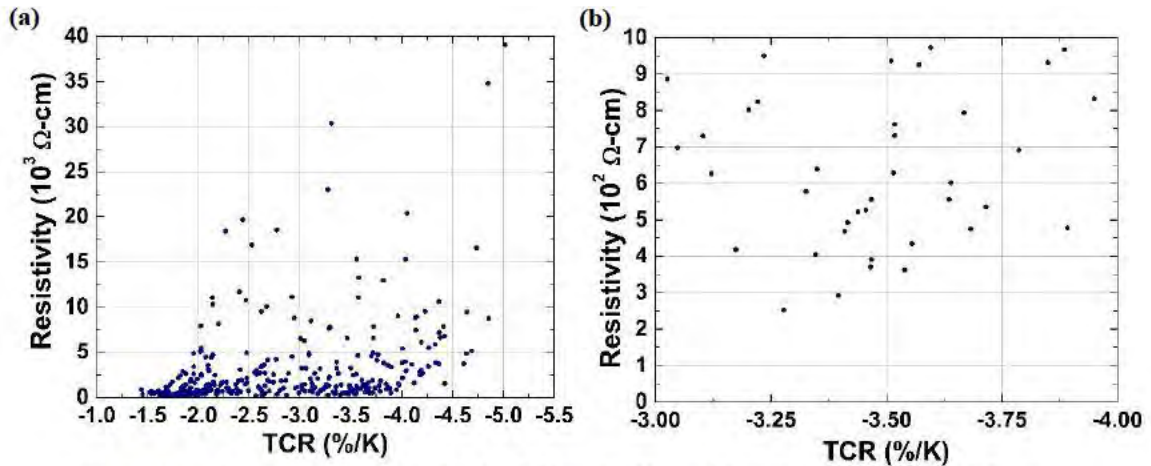

Figure 4: Resistivity versus TCR for a) all films, b) films with resistivity below 1.0 kΩ-cm.

TCR and Resistivity as a function of Silicon concentration

The effect of O_2 on TCR, and resistivity of $Si_xGe_yO_{1-x-y}$ films were measured as a function of Si concentration, for a low level of O_2 concentration between 1 to 10% and is shown in Figure 6. The atomic composition of O_2 was fixed to a very small range since we were not experimentally able to fix the O_2 content in the film into an exact single number. This is due to changes of the bonding between oxygen to silicon and germanium during the sputter-deposition. The experimental results were interpreted and explained as follow: (1) The O_2 atomic composition was fixed between 3.36% and 3.89% while Si concentration was varied (Figure 6a, and 6b). The figure shows that as the Si composition was increased from 3% to 20% the TCR was changed slightly between –1.754 %/K and –2.018 %/K while the resistivity
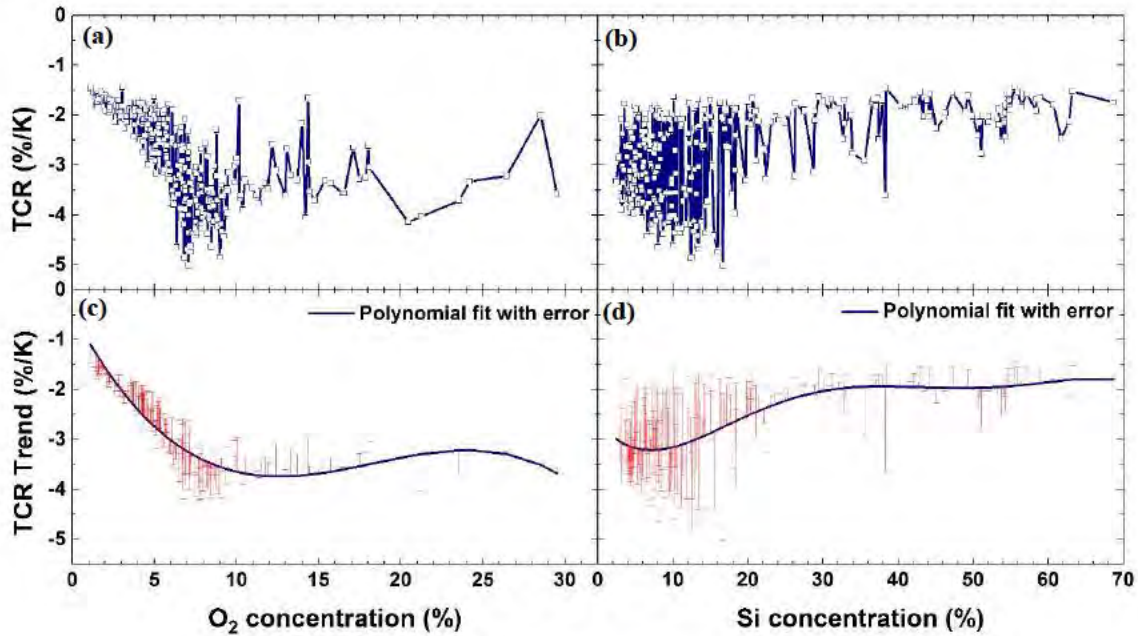

Figure 5: TCR trend with respect to element concentration in $Si_xGe_yO_{1-x-y}$ using polynomial fit

value was around 119.6 Ω-cm. The activation energy (E_a) was found to be stable around 0.142 eV. However, as the silicon content increased above 20% the resistivity value increased by 10 times to 1.25 kΩ-cm while TCR stayed in the same range. (2) As the O_2 concentration was increased to 4% - 4.97%, the TCR value was increased to a value around –2.0%/K. The highest measured TCR and the corresponding resistivity were –2.48 %/K and 1.64 kΩ-cm at a Si concentration of 37.4%, respectively. The activation energy was changed between 0.1232 eV and 0.1906 eV. The general trend is that the TCR was relatively stable around –2.0 %/K. The resistivity value was mostly below 1 kΩ-cm when the Si concentration was below 16%. It was increased as the Si concentration was increased above 16 % while TCR stayed in the same range (See Figure 6c, and 6d). (3) As the O_2 concentration was increased to 5% – 5.48%, and as the Si in increased up to 6.5%, the TCR was increased to –3.174 %/K while the resistivity stayed relatively constant below 1 kΩ-cm. The corresponding resistivity for the highest TCR was 418 Ω-cm. As the Si concentration increased further up to 11%, the TCR was decreased and stayed stable afterwards around –2 %/K, and resistivity was relatively increased (Figure 6e, and 6f). At this oxygen concentration, we have observed a few data points with high TCR and with corresponding low resistivity values. We have also observed a couple of data points where TCR was around –2 %/K but the resistivity was very high. (4) As the O_2 concentration was increased to 6.04% – 6.97%, the TCR values in general was increased up to –4%/K for Si concentration between 3% – 7% (Figure 6g, and 6h). We have

observed several data points with high TCR and corresponding low resistivity values. As the Si is increased further to 12%, the TCR and resistivity were increased up to –5 %/K, and 8.75 kΩ-cm, respectively. Above 12% the TCR was dropped to value around –3%/K, while the resistivity in general was increased with the exception of couple of data points. (5) As the Si concentration was increased above 7% for a fixed O_2 concentration between 7.03% – 7.95%, the TCR was increased with the highest was –5.017 %/K and 39.07 kΩ-cm at 10% Si concentration. As the Si concentration was increased above 10%, the TCR was decreased while the resistivity kept on increasing trend (Figure 6i, and 6j). (6) We had a similar observation when the O_2 was increased to 8.09 –8.99%. In this case, the TCR was stabilized at –4%/K while the resistivity kept in increasing as Si concentration increases above 7% (Figure 6k, and 6l). (7) When the O_2 was increased to 9.04 – 9.93%, the TCR was increased and stabilized at a value around –4.2 %/K with the exception of one data point while the resistivity was kept on increasing as Si concentration was increased above 6%. However, we did not measure their behavior at higher Si concentration at this time. We observed that at low Si concentration, several data points have high TCR and low resistivity values (Figure 6m, and 6n). (8) A similar trend was observed in (Figure 6o, and 6p) as the Si concentration was increased above 5.5%. As a conclusion, the results indicates that for low fixed O_2 concentration below 5%, the TCR and resistivity changes were not affected significantly by the changes of Si concentration until it increases above 16%. On the other hand, as the fixed O_2 concentration was increased above 5%, the TCR and resistivity started to be affected by the Si concentration. We observed that the TCR increases as Si composition increases to a specific value (e.g., 8% in case of 6f) and then drop a little bit and then stabilize. We also observed that this specific Si concentration value was dropped from 8% to 5% as the fixed O_2 was increased.
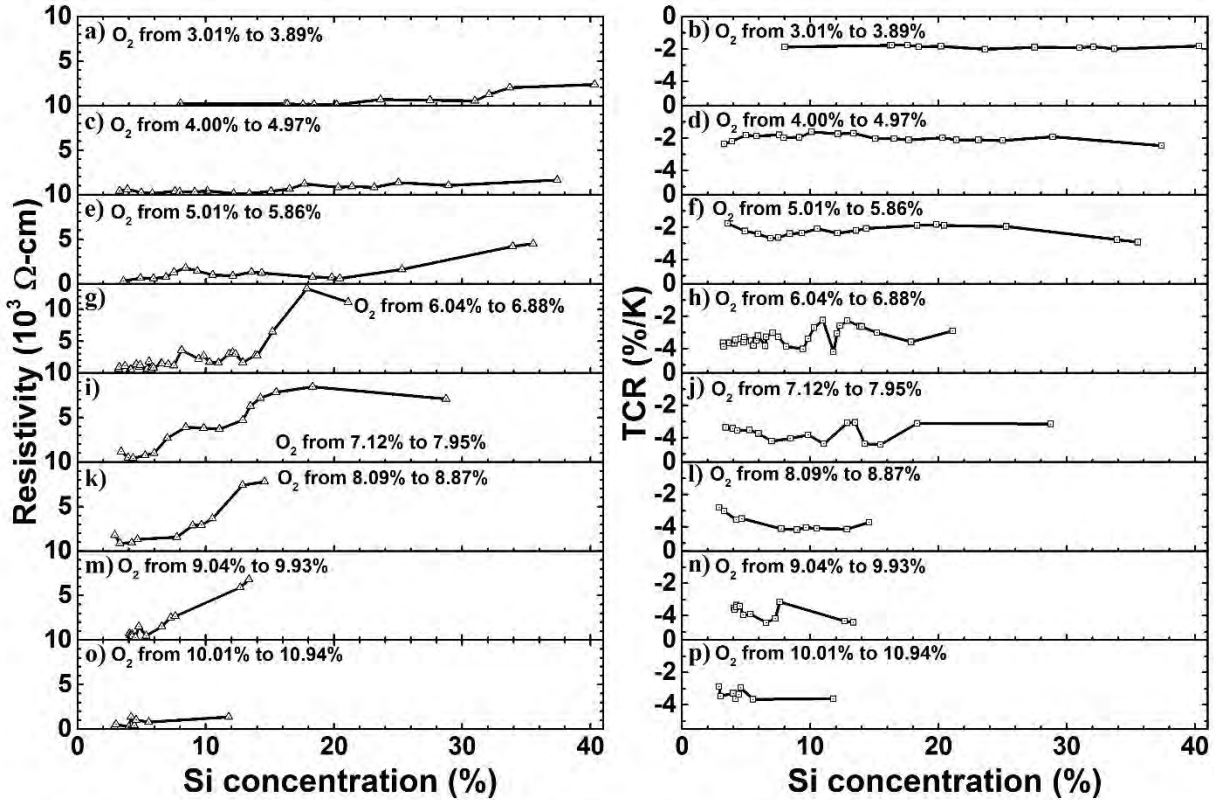

Figure 6: Resistivity and TCR as a function of Si concentration for a fixed O_2 (a-b) 3.01-3.89%, (c-d) 4.00-4.97%, (e-f) 5.01-5.86%, (g-h) 6.04-6.88%, (i-j) 7.12-7.95%, (k-l) 8.09-8.87%, (m-n) 9.04-9.93%, (o-p) 10.01-10.94%

TCR and Resistivity as a function of Oxygen concentration

The effect of Si on TCR, and resistivity of $Si_xGe_yO_{1-x-y}$ films were measured as a function of O_2 concentration, for Si concentration between 3% - 18% and is shown in Figure 7. Again, the atomic composition of Si was fixed to a very small range since we were not experimentally able to fix the Si content in the film into an exact single number. (1) The Si concentration was fixed between 3.00% − 3.95%, and as the O_2 concentration was increased to 8%, the TCR was increased to −3.4 %/K. As the O_2 concentration was increased above 10.5%, the TCR was dropped to −3.1 %/K with few exceptions. The resistivity was fluctuating between 370 Ω-cm and 2.06 kΩ-cm, with increasing trend at higher O_2 concentration. The Ea was changed from 0.16587 eV to 0.2861 eV (See Figure 7a, and 7b). (2) As the Si concentration was fixed to 5.04% − 5.92%, the TCR was gradually increased from −1.9 %/K to −3.9 %/Kas the O_2 concentration increases. Above an O_2 concentration of 10.4%, the TCR was decreased stayed relatively constant around −3 %/K. At that level of O_2 concentration the resistivity was increased too to a higher value under 1 kΩ-cm to over 3 kΩ-cm. We had a few data point where the TCR was above
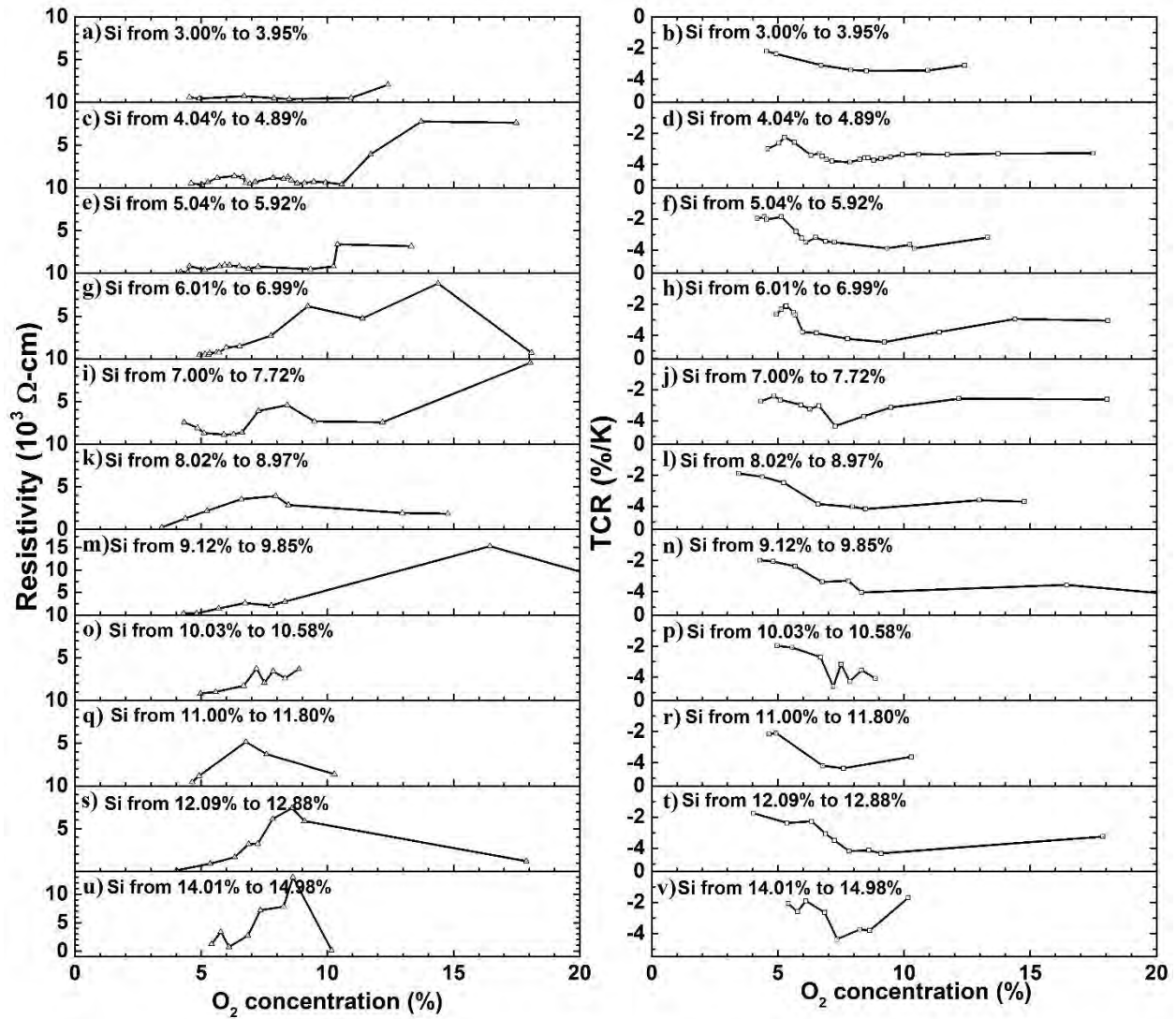

Figure 7: TCR and Resistivity as a function of O_2 concentration for fixed Si of (a-b) 3% to 3.95%, (c-d) 4.00% to 4.89%, (e-f) 5.04% to 5.92%, (g-h) 6.01% to 6.99%, (i-j) 7.00% to 7.72%, (k-l) 8.02% to 8.97%, (m-n) 9.12% to 9.85%, (o-p) 10.03% to 10.58%, (q-r) 11% to 11.8%, (s-t) 12.09% to 12.88% and (u-v) 14.01% to 14.98%.

12

–3.5%/K and the resistivity were below 1 kΩ-cm. The Ea was changed in between 0.14197 eV and 0.294 eV (See Figure 7e, and 7f). (3) Similar behavior was observed as the Si concentration was fixed at 6.01% - 6.99%, and as the O_2 increased to 9.22%, the TCR was increased to –4.42%/K. The TCR value was then dropped to a value around –3%/K stayed relatively constant, while the resistivity was increased from 460 Ω-cm to 8.8 kΩ-cm. The corresponding Ea changed its value in between 0.15795 eV and 0.3339 eV (See Figure 7i, and 7j).

(4) Similar behavior was observed as the Si concentration was fixed at 7% - 7.72%, and as the O_2 increased to 7.27%, the TCR was increased –4.33 %/K. The TCR value was then dropped around –2.6 %/K and stayed relatively constant, while the resistivity was increased from as low as 1.1 kΩ-cm to 9.5 kΩ-cm. The corresponding E_a changed its value in between 0.18298 eV to 0.32725 eV (See Figure 7i, and 7j). (5) Similar behavior was observed at higher fixed Si concentration of 8% - 8.97%. As the O_2 concentration was increased to 7.95%, TCR was increased to –4.04 %/K and then dropped to –3.6 %/K and stabilized. On the other hand the resistivity was always on an increasing trend as the O_2 concentration increased (See Figure 7k, 7l). (6) the high oxygen value follow similar trend (see Figure 6m-6v). The results indicates that an O_2 concentration around 6% to 8% is needed to achieve highest TCR, and relatively low resistivity value. Below this value, the TCR was always lower. Above this value, the TCR tend to drop and stabilizes at lower value, and the resistivity tend to increase to a higher value. It is also important to note that there are several point where the TCR was high while the corresponding resistivity was low. Further study needs to be conducted at higher Oxygen concentration.

X-Ray Diffraction (XRD) measurements

The crystalline structures of $Si_xGe_yO_{1-x-y}$ thin films were identified using X-Ray diffraction (XRD). A

diffractometer (Rigaku - Ultima IV XRD system) is used for this purpose varying 2θ from $0°$ to $60°$. The

first set of measurements were performed for films with a fixed O_2 concentration while Si was varied

from 1% to 20%. Figure 8(a),(b) shows the XRD for fixed O_2 of 4% and 8%. We have not observed any

sharp peak in the spectrum, suggesting amorphous nature of all films. The dominant partial diffraction

peak of (111) (peak 01) was located approximately at 27°. The full width at half maximum (FWHM) for

this peak did not show any significant broadening or narrowing. At a fixed O_2 concentration of 4.13%-

4.92%, the second peak shift around 48° (crystal plane (220), referred as peak 02) and spectrum

broadening with respect to changes in Si concentration was small and comparable (See Figure 9(a)). This

has resulted in a lower TCR value (around –2.3 %/K) that has small changes as a function of Si

composition (See Figure 10(a)). For a fixed O_2 concentration of 8.39%-8.99% and at higher 2θ around

48$^{\text{o}}$, we have observed a peak shift and broadening in the spectrum as the Si concentration increased to 5-

6%, and then they decreased and stabilized as the Si concentration increased further (See Figure 9(a)).

The peak shift and peak broadening were plotted as a function of TCR and resistivity in Figure 10. The

figure shows that as the FWHM increased, the TCR value was decreased. This can be related to the

increase of TCR as the Si concentration increased up to a certain value (e.g., 6%), and then decreased and

stabilized as the Si concentration increased further. The maximum achieved TCR was −5.6 %/K at a

FWHM of 5° for the peak 02 (Figure 10(d)). The TCR was stabilized around –3.8 %/K at FWHM above

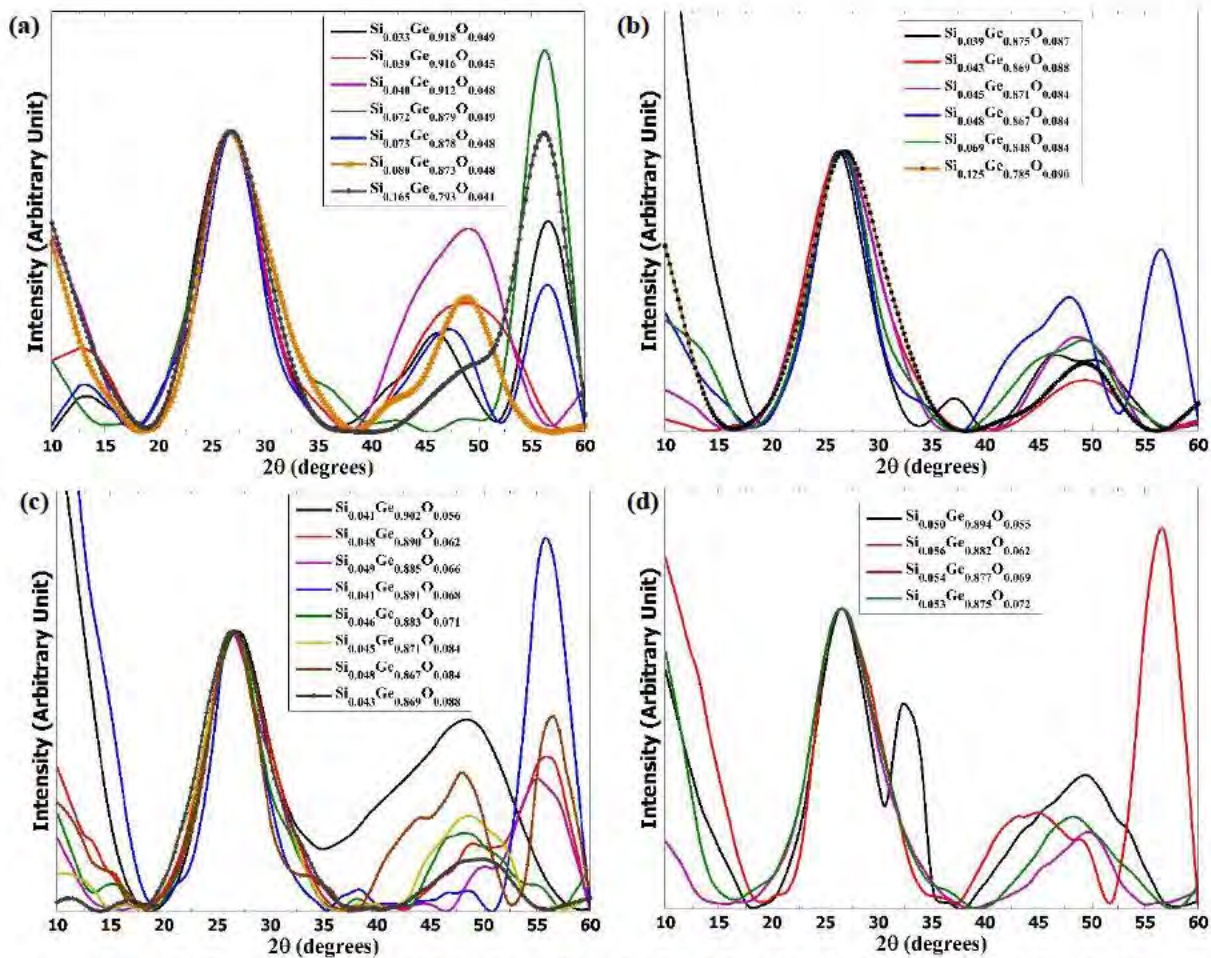8° (Figure 10(d)). The figure also shows that as the peak shift increased to 48° the TCR reached a

Figure 8: X-ray diffraction of $Si_xGe_yO_{1-x-y}$ films for fixed O_2 a) 4%, b) 8%., fixed Si c) 4%, d) 5%.
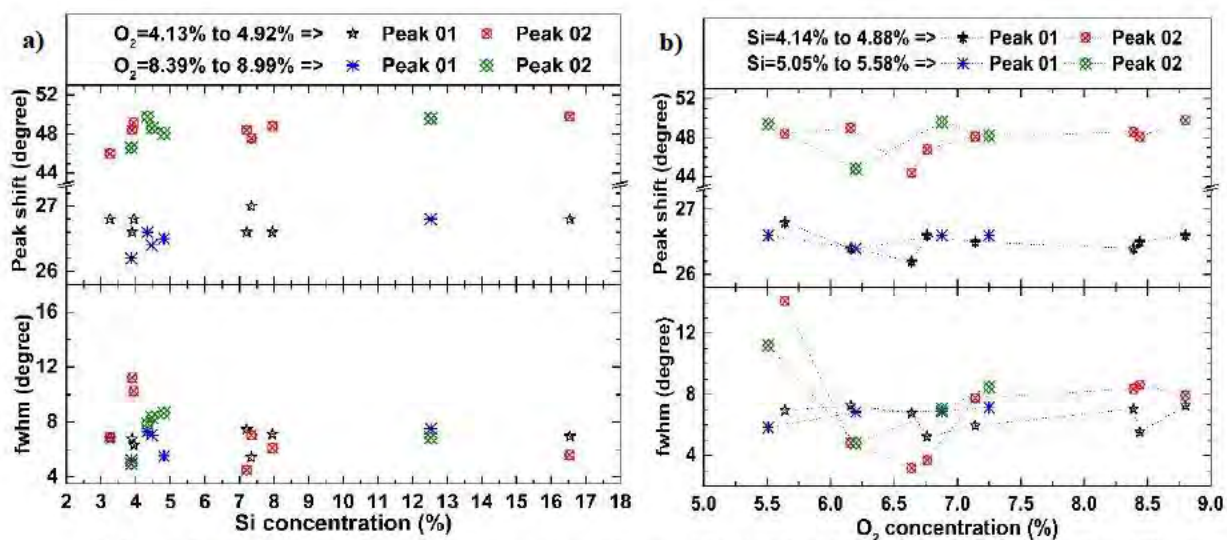

Figure 9: XRD Peak shift and fwhm vs element concentration for a) fixed O_2 (4%, 8%) b) fixed Si (4%, 5%)

minimum value of –3.5%/K and then starts to increase again to a value above –5 %/K at 48.8° (Figure

Figure 10: Resistivity and TCR vs Peak shift of films for fixed O$_2$ (a) peak at (111) (c) peak at (200); Resistivity and TCR vs fwhm of films for fixed O$_2$ (a) peak at (111) (c) peak at (200)

10(c)). This behavior agrees with the TCR plots as a function of Si composition for fixed O$_2$ contents in Figure 6. The first peak shift and FWHM was also plotted as a function of TCR in Figure 10 (a), (b). The figure shows that as the peak shift to a higher value the TCR decreases. At 26.5°, the TCR was decreased to −3.5 %/K. As the peak shift increases further, the TCR value was increased again. The FWHM shows
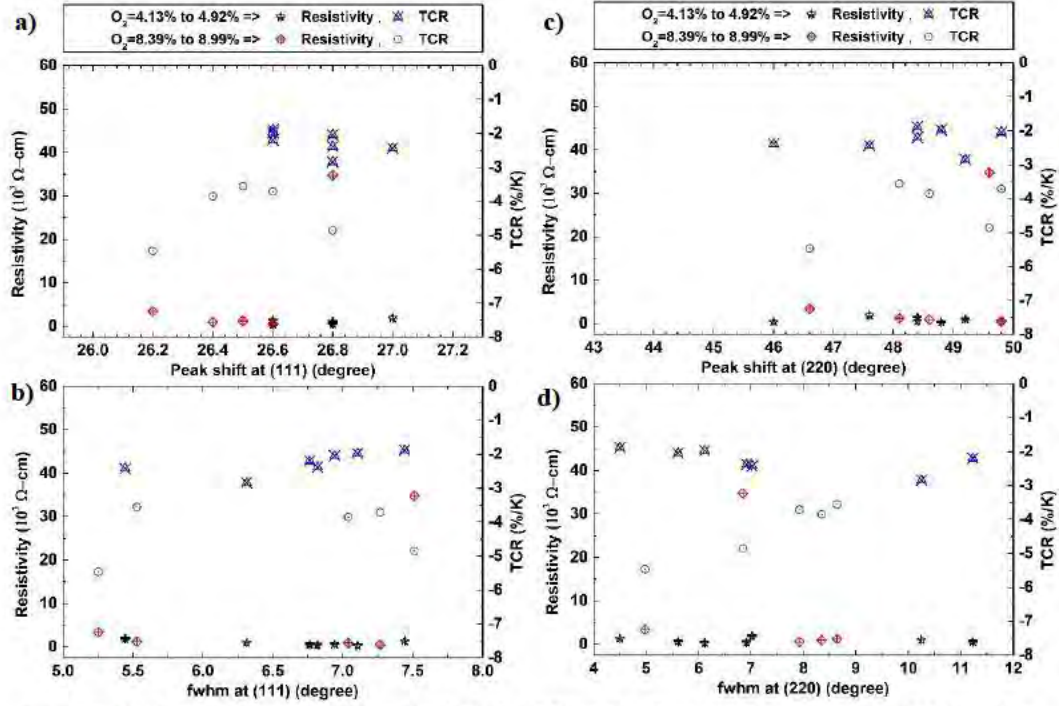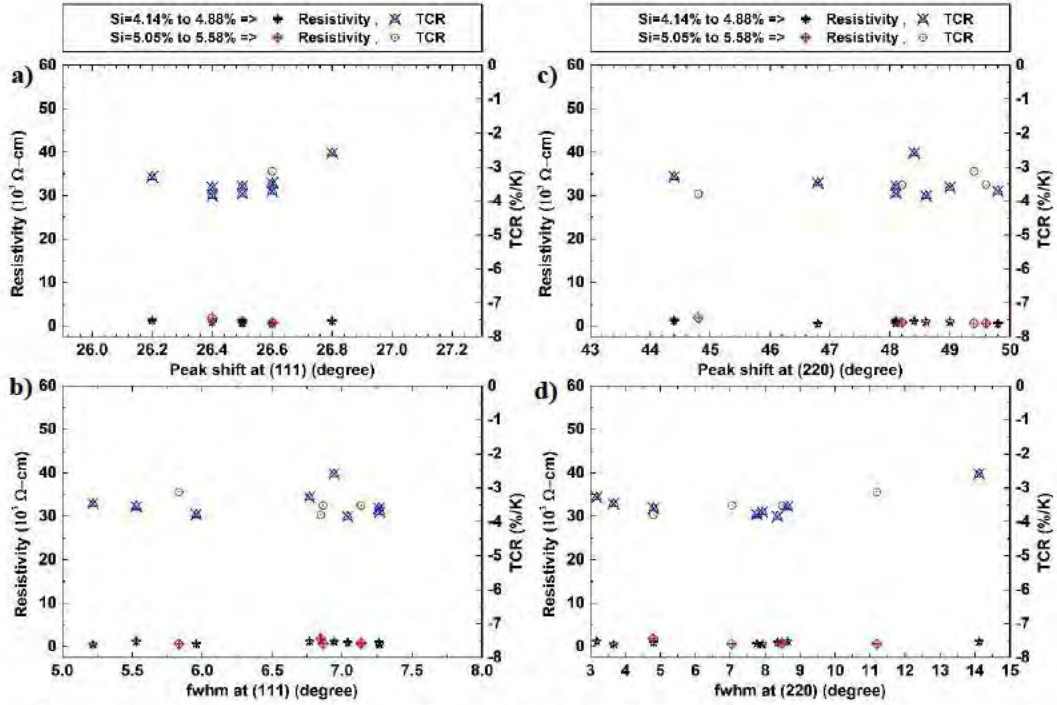

Figure 11: Resistivity and TCR vs Peak shift of films for fixed Si (a) peak at (111) (c) peak at (200); Resistivity and TCR vs fwhm of films for fixed Si (a) peak at (111) (c) peak at (200)

broadening and then stabilizing. The last data did not follow the trend and it is an exception. The results of the first peak shift and FWHM was also plotted as a function of TCR, the results shows similar behavior, as the peak shift to a higher value the TCR decreases. At 26.5°, the TCR was decreased to –3.5 %/K. As the peak shift increases, the TCR value was increased again. The FWHM shows broadening and then stabilized. The last data point was an exception.

We have also plotted the XRD for fixed Si concentration of 4% and 5% while the O_2 was varied between 4% to 9 % (Figure 8(c),d)). The figure demonstrates that the FWHM of the second peak was initially decreased as the O_2 conentration increased to 7% and then increased gradually and stablized. This results is in ageement with the data presented in Figure 7 for the range 5% - 9%. We have also plotted the corresponding the peak shift and FWHM as a fucntion of TCR and resistivity (see Figure 11). The figure indicates that as the peak shift or FWHM increases, the TCR changed slightly around -3.8%/K which is in agreement with the results in Figure 7. At FWHM of 15, the TCR is the lowest. We do not have enough data at higher O_2 concentration to confirm the trend. The corresponding data for these measurements are shown in Table 3 and Table 4.

Table 3. TCR, Resistivity and Activation energy of samples corresponding to
XRD spectra in Figure 8 (a) and (b)

Oxygen Concentration	Film Composition	Resistivity ($\times 10^3 \Omega$-cm)	TCR (Calculated) (%/K)	Activation Energy Ea (eV)
$O_2 = 4\%$	$Si_{0.033}Ge_{0.918}O_{0.049}$	0.442	–2.381	0.1798
	$Si_{0.039}Ge_{0.916}O_{0.045}$	0.6124	–2.197	0.1659
	$Si_{0.040}Ge_{0.912}O_{0.048}$	1.0270	–2.839	0.2144
	$Si_{0.072}Ge_{0.879}O_{0.049}$	1.4080	–1.877	0.1417
	$Si_{0.073}Ge_{0.878}O_{0.048}$	1.8870	–2.424	0.1830
	$Si_{0.080}Ge_{0.873}O_{0.048}$	0.3089	–1.972	0.1489
	$Si_{0.165}Ge_{0.793}O_{0.041}$	0.6332	–2.041	0.1584
$O_2 = 8\%$	$Si_{0.039}Ge_{0.875}O_{0.086}$	3.3975	–5.463	0.2080
	$Si_{0.043}Ge_{0.869}O_{0.088}$	5.3517	–3.715	0.2810
	$Si_{0.045}Ge_{0.871}O_{0.084}$	9.3136	–3.850	0.2910
	$Si_{0.048}Ge_{0.867}O_{0.085}$	1.2360	–3.557	0.2690
	$Si_{0.125}Ge_{0.785}O_{0.090}$	3.4778	–4.848	0.3660

Raman spectroscopy

Raman scattering spectra of Si-Ge-O for fixed oxygen of 3 %, 4 %, 5%, 6 %, 7%, 8%, 9% and 10% with varying silicon content were measured and analyzed for Raman shift from 100 cm^{-1} to 600 cm^{-1}. The spectra for 5% and 7% are shown in Figure 12. This study will provide us with a better understanding of the effects of varying Si, Ge, and O compositions on the bonding between Si-Ge, and Ge-Ge, and its effects on TCR and resistivity. The plots of all samples demonstrate peaks around 275 cm^{-1} (peak 1) and 400 cm^{-1} (peak 2) which correspond to Ge-Ge, and Ge-Si bonding, respectively. The Ge-Si was not noticeable at low level of Si atomic % but as the Si atomic % increases the Ge-Si starts to appear. The Ge-Ge bond appears to be strong due to the high concentration of Ge in the film.

The Ge-Ge bonding peak shift and Ge-Si bonding peak shift are plotted as a function of Si concentration for a fixed O_2 concentration of 4%, 5%, 6% and 8% in Figure 13. The results demonstrate that for a fixed O_2 of 4% and for low Si concentration below 10% the Ge-Si bonding peak shift and the Ge-Ge bond shift are relatively small, which can be related to the relatively stable value of resistivity and TCR at this concentration range. As the Si increased further, the resistivity increased due to the increase of Si in the film, and the TCR was relatively stayed stable due to the small Ge-Ge peak shift. For a fixed O_2 of 8% and for low Si concentration below 10%, the Ge-Ge bonding peak shifts increased which explains the increase in TCR. On the other hand, the Ge-Si slightly changed which also explain the small change in resistivity in the same range. As the Si concentration increased further, Ge-Si peak shift to a higher value explaining the large increase in resistivity, the Ge-Ge peak shift has increased slightly which explains the relatively stable TCR as the Si concentration increased.

It is evident in Figure 13 that with the increase of Si concentration Ge-Si bonding peaks shifts more towards Si-Si bonding around 521 cm^{-1} irrespective of O_2 concentration. Similar pattern peak movement was observed for Ge-Ge peak as Si concentration increase for low O_2 of 4%. But as the O_2 concentration increase this peak shift changes its direction for increasing Si concentration.
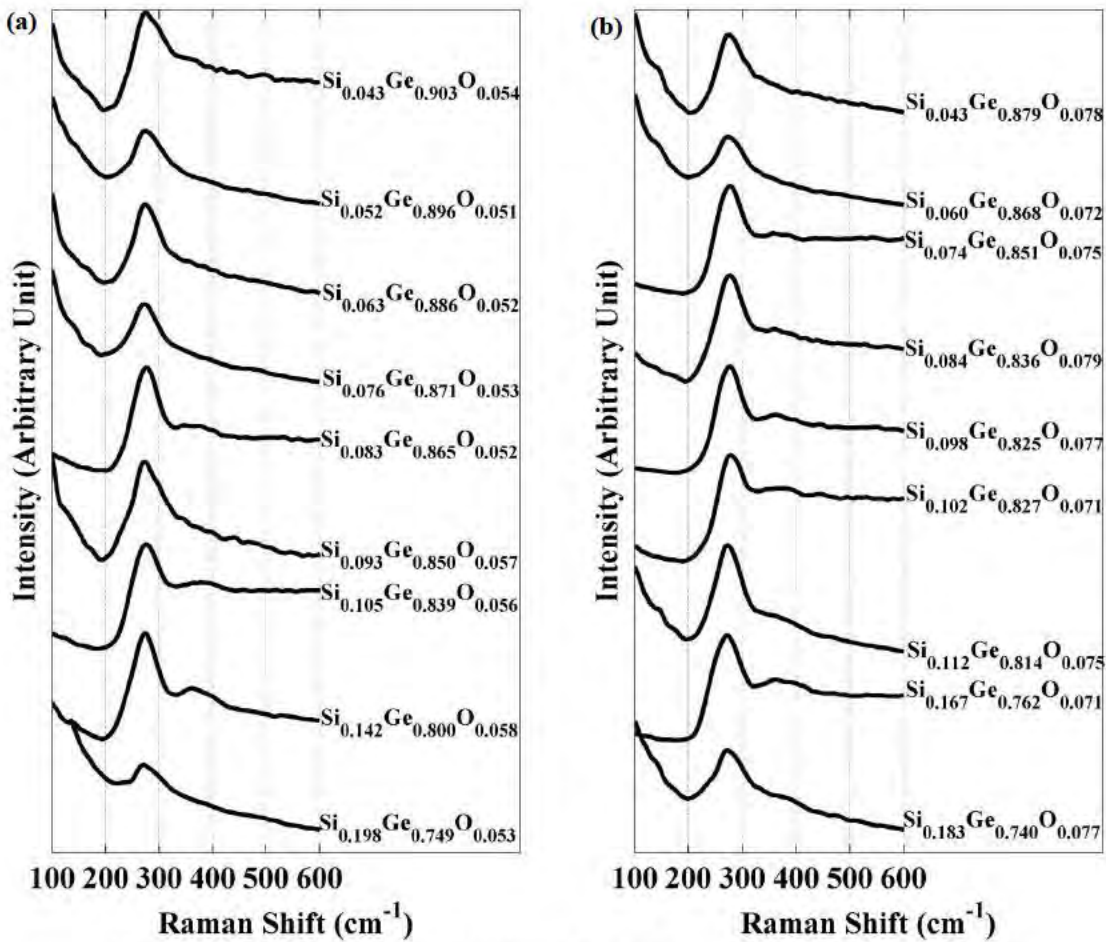

Figure 12: Raman spectra of $Si_xGe_yO_{1-x-y}$ films with oxygen content of (a) 5%, (b) 7%

Table 4. TCR, Resistivity and Activation energy of samples corresponding to XRD spectra in Figure 8 (c) and (d)

Silicon Concentration	Film Composition	Resistivity $(\times 10^3 \Omega\text{-cm})$	TCR (Calculated) (%/K)	Activation Energy Ea (eV)
Si = 4%	$Si_{0.041}Ge_{0.902}O_{0.057}$	1.170	−2.590	0.1956
	$Si_{0.048}Ge_{0.890}O_{0.062}$	0.973	−3.596	0.2716
	$Si_{0.049}Ge_{0.885}O_{0.066}$	1.259	−3.285	0.2480
	$Si_{0.041}Ge_{0.891}O_{0.068}$	0.556	−3.468	0.2636
	$Si_{0.046}Ge_{0.883}O_{0.071}$	0.691	−3.787	0.2859
	$Si_{0.045}Ge_{0.871}O_{0.084}$	0.931	−3.850	0.2910
	$Si_{0.048}Ge_{0.867}O_{0.085}$	1.236	−3.557	0.2690
	$Si_{0.043}Ge_{0.869}O_{0.088}$	0.535	−3.715	0.2810
Si = 5%	$Si_{0.051}Ge_{0.894}O_{0.055}$	0.627	−3.121	0.2360
	$Si_{0.056}Ge_{0.882}O_{0.062}$	1.829	−3.792	0.2863
	$Si_{0.054}Ge_{0.877}O_{0.069}$	0.629	−3.516	0.2650
	$Si_{0.053}Ge_{0.875}O_{0.072}$	0.763	−3.518	0.2656
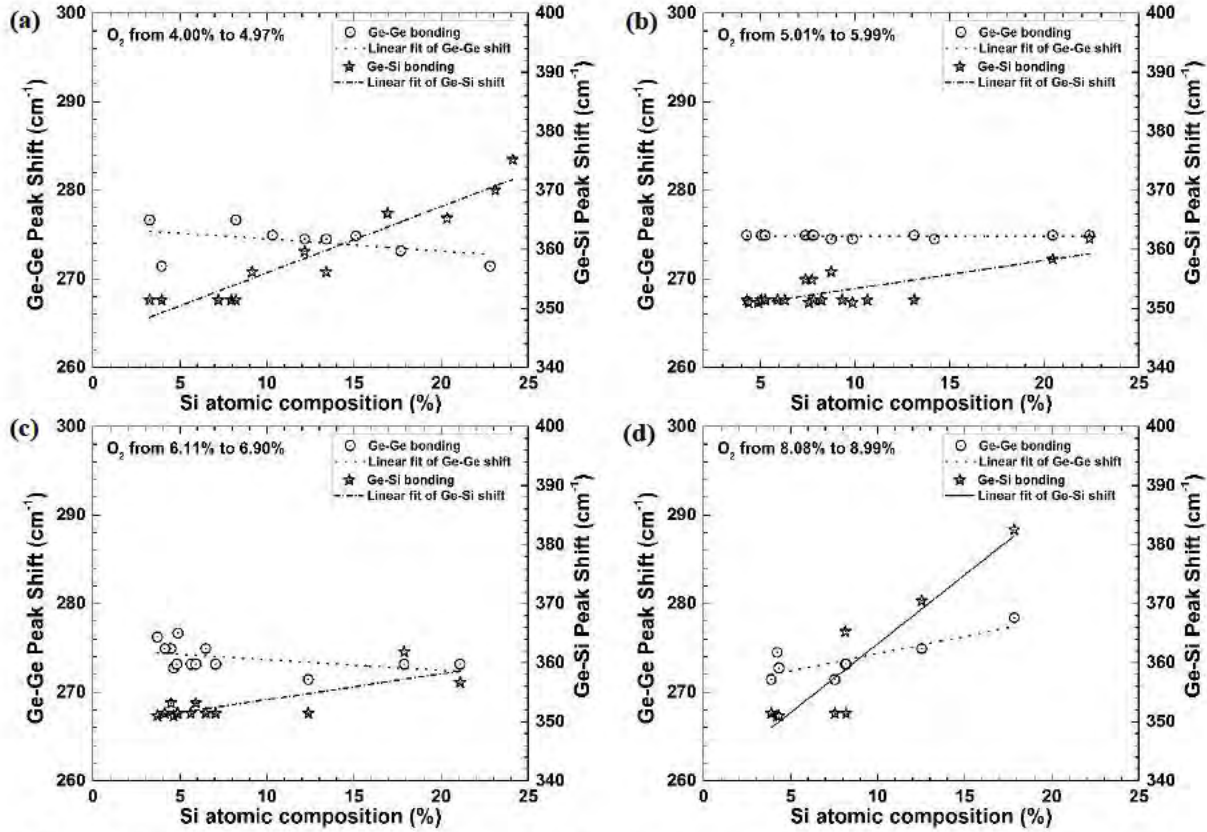
Figure 13: Peak shift of Ge-Ge bonding and Ge-Si bonding as a function of Si concentration for fixed O_2 of (a) 4%, (b) 5%, (c) 6% and (d) 8%

Fourier transform infrared spectroscopy (FTIR)

To further investigate the electrical properties of the films, FTIR spectra were recorded using Nicolet 4700 FT-IR spectrophotometer between 400 cm^{-1} to 4000 cm^{-1}. The lattice phonon contributions of Si wafer background were subtracted. In this experiment, we have fixed the oxygen and varied the silicon concentration. The FTIR spectra are shown in Figure 14. A major Absorption peak corresponding to Si-O

Figure 14: FTIR spectra for oxygen content (a) 5%, (b) 6%, (c) 7% and (d) 8%

is located around 960 cm^{-1} for all samples with very few exceptions. The Ge-O bonds was observed at around 800 cm^{-1} for samples with oxygen concentration higher than 6%. We were not able to relate the TCR and resistivity behavior of Si-Ge-O with FTIR spectra.

Microbolometer Design and Device Fabrication

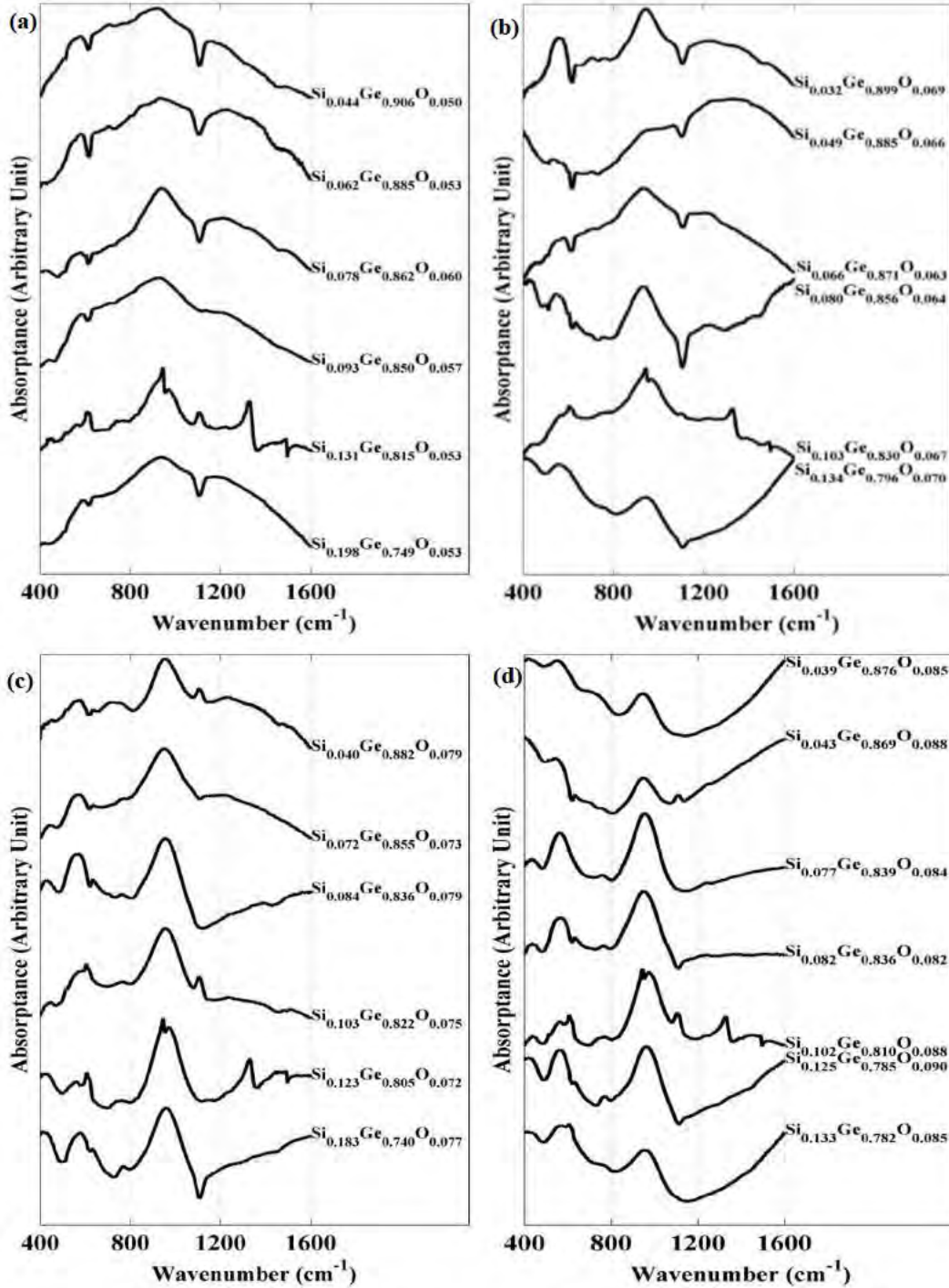The microbolometer is designed with pixel sizes of 25×25 µm^2 and 40×40 µm^2 for long wavelength detection based on Si$_{0.041}$Ge$_{0.868}$O$_{0.091}$ composition which provides relatively high TCR and low resistivity values of −3.64 %/K and 5.564 ×10^2 Ω cm, respectively (See Figure 15). It consists of a thin Si$_3$N$_4$ bridge suspended above a silicon substrate as shown in Figure 15. The bridge is supported by two narrow arms of Si$_3$N$_4$ and NiCr films. The arms serve as support structure, conductive legs and thermal isolation legs. Encapsulated in the center of the Si$_3$N$_4$ bridge is a thin layer of Si-Ge-O IR sensitive material and thin titanium (Ti) absorber. The Si$_3$N$_4$ was chosen for its excellent thermal properties, processing characteristics and high infrared absorption. The Si-Ge-O IR sensing layer was fabricated on top of polyimide sacrificial layer. Subsequent etching of the sacrificial layer provides the air gap that thermally isolates the microbolometer. A Au thin film was fabricated of gold (Au) layer under the polyimide sacrificial layer to act as a mirror for the resonant cavity between the mirror and Si-Ge-O thin film layer. This optical resonant cavity plays an important role in the absorption of infrared radiation for the suspended microbolometer since it is wavelength dependent. With the appropriate design, the resonant cavity maximizes the IR absorption and hence maximizes the responsivity with an absorption peak in the long wavelength band. The resonant cavity can be created between the incoming and reflected waves if the cavity depth is tuned accordingly: $d_n = [(2n-1)-(\varphi_1 - \varphi_2)]\lambda/4$, where d_n is the depth of the air gap, n is an integer, λ is the wavelength and φ_1, and φ_2 are the phase differences between the incoming and
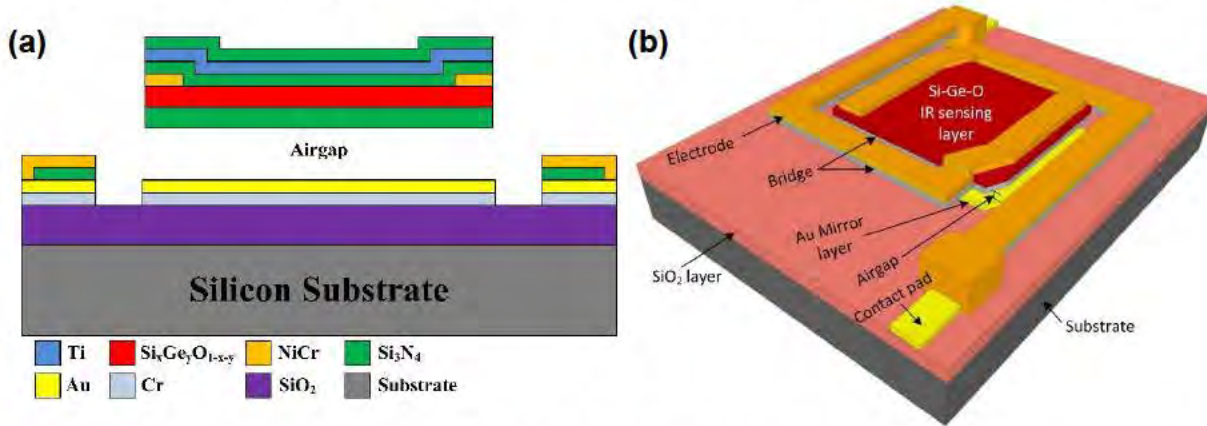
Figure 15: Uncooled microbolometer design with airgap, **a)** Cross-sectional view having polyimide sacrificial layer, **b)** 3-dimensional view after releasing of polyimide.
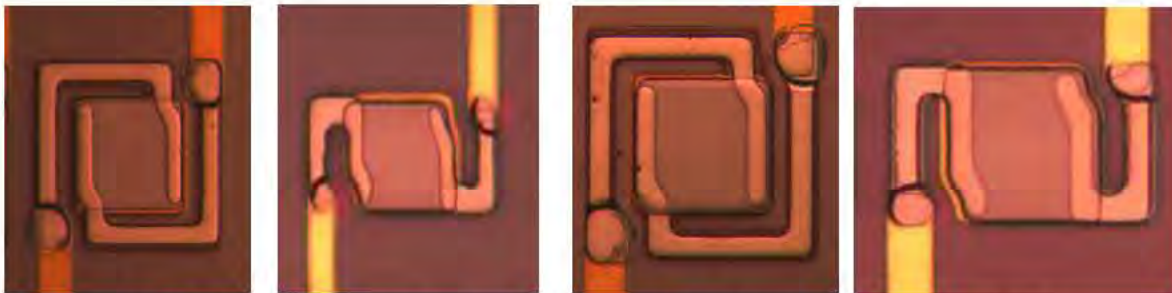
Figure 16: Optical images of the microbolometer with a pixel area of 25×25 µm^2 and 40×40 µm^2 after removing the polyimide sacrificial layer

reflected light [11].

The microbolometer was fabricated using a series of photolithography, surface micromachining and polyimide sacrificial layers in the following sequence of steps (Figure 18). 1) The wafer was thermally oxidized for insulation. 2) A thin layer of chromium (Cr) and a thin layer of gold (Au) were sputtered deposited with a thickness of 30 nm and 140 nm, respectively, and patterned to form the reflective mirror under the microbolometer pixel, the trace line and bonding pads. 3) A polyimide (PI2610) sacrificial layer was spin coated and cured to achieve a thickness of 2 µm, and patterned to create a mold at locations
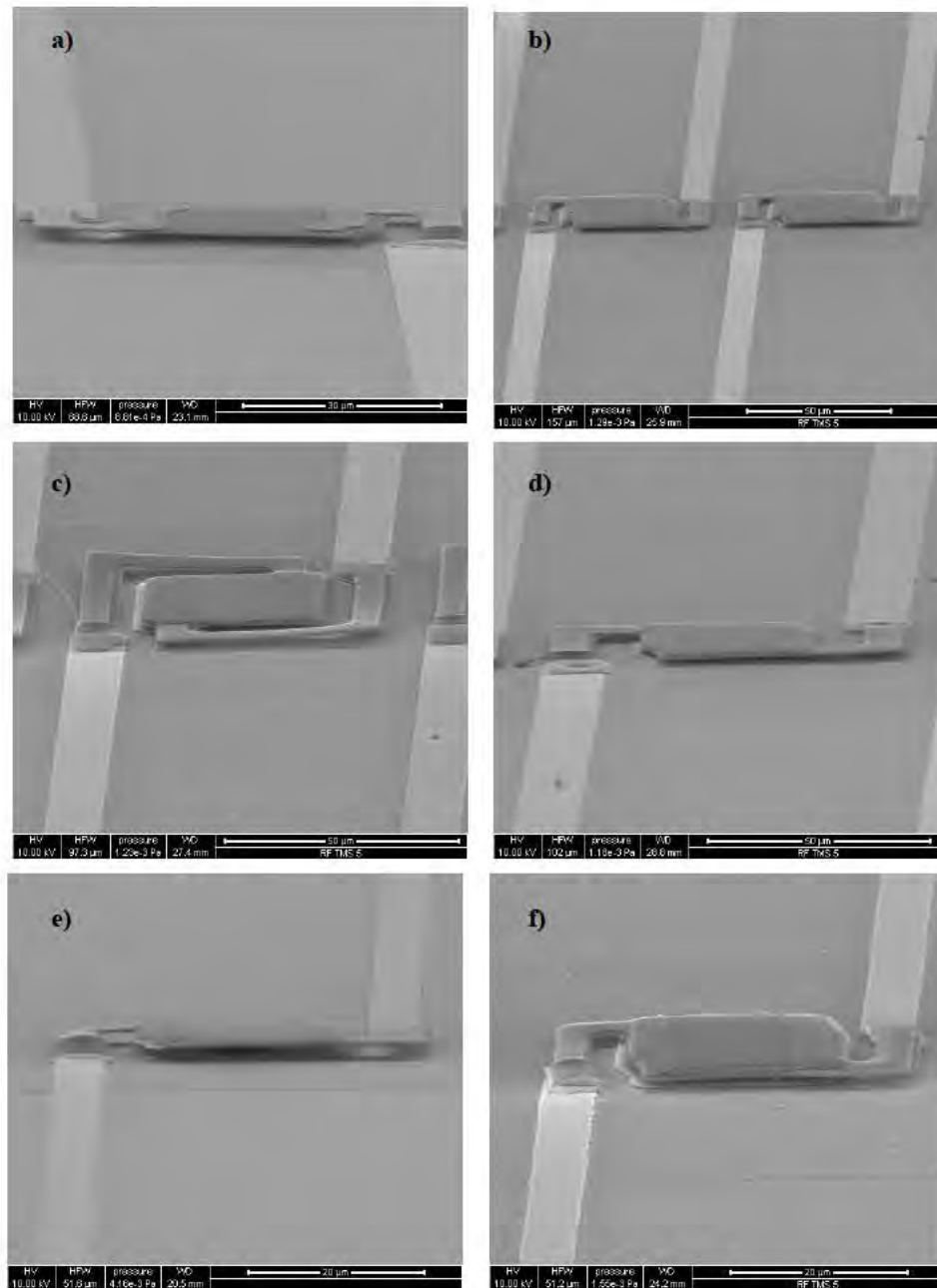
Figure 17: SEM micrographs of the microbolometer after removing the polyimide sacrificial layer with a pixel area of a-d) 40×40 µm^2, e, f) 25×25 µm^2.

corresponding to the microbolometer anchors. Photoresist was patterned used as a mask for etching polyimide, and polyimide was etched using reactive ion etching system. 4) A layer of Si_3N_4 (300 nm) was sputter-deposited and patterned as a bridge. 5) The Si-Ge-O thermometer layer (300 nm) was sputter deposited and patterned. 6) NiCr layer (100 nm) was deposited and patterned to form the supporting/conductive arms. 7) A second layer of Si_3N_4 (50 nm) was deposited and patterned for insulation followed by sputtering of a thin Ti absorber (5 nm), and another Si_3N_4 (50 nm) for passivation. 8) The top two
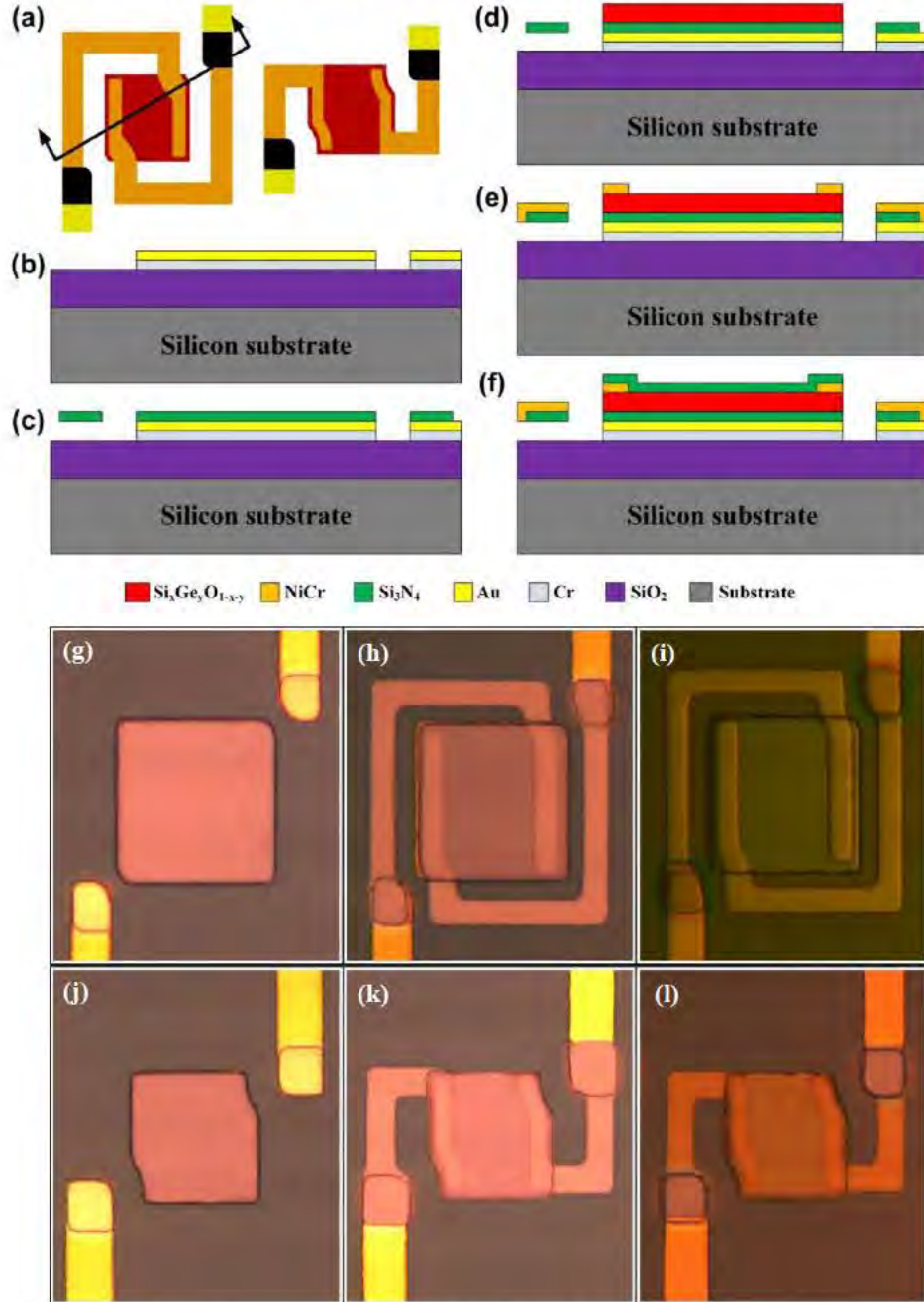
Figure 18: Microbolometer fabrication steps: (a) Top view of pixels of two designs with different supporting arm structure; (b) Cross sectional view of different steps of fabrication. Optical images of the microbolometer with a pixel area of 40×40 μm² at the end of different steps of fabrication, g) Si-Ge-O layer, h) Ni-Cr layer, i) final device for L-shaped anchor; j) Si-Ge-O layer, k) Ni-Cr layer, l) final device for I-shaped anchor

Si$_3$N$_4$ layers and NiCr absorber were patterned using lift off process. 15) The polyimide sacrificial layers are removed by oxygen plasma ashing. Optical images and SEM micrographs are shown in Figure 16 and Figure 17.

Noise measurement setup and results

The microbolometers were fabricated without an air gap for the purpose of studying voltage noise (PSD) of Si$_x$Ge$_y$O$_{1-x-y}$ thin films encapsulated with Si$_3$N$_4$ layers. The elimination of the air gap will speed up the fabrication processes of many devices with various elemental compositions. The film composition and corresponding electrical characteristics are in Table 5. The microbolometers were fabricated with a pixel area of 25×25 μm^2 and 40×40 μm^2 on top of oxidized silicon substrates using surface micromachining processes. A top view of two different type of supporting arm structure is shown in Figure 18(a). Cross-sectional views of different steps of the fabrication of the device is shown in Figure 18(b-f). We have used RF magnetron sputtering for all deposition at 4 mTorr with a base pressure of below 10^{-7} Torr, and lift-off process for patterning all films. The microbolometers were fabricated in the following sequence: 1) the wafers were thermally oxidized (0.6 μm) for insulation, 2) two layers of chromium (Cr) and gold (Au) with thickness of 50 nm, and 100 nm, respectively, were sputtering deposited (Figure 18(b)). Cr serves as an adhesion layer for Au. The Au layer was patterned to form the trace line and bonding pads. A reflective mirror was also patterned under the pixel but was not needed for this study, 3) A Si$_3$N$_4$ layer with a thickness of 100 nm was sputter deposited and patterned for passivation from the bottom side (Figure 18(c)), 4) The Si-Ge-O thermometer layer was then deposited with a thickness of 300 nm and patterned (Figure 18(d)), 5) Nickel-chromium layer (Ni-Cr) with a thickness of 60 nm was deposited and patterned to create the arms and electrode contacts to the sensitive IR material (Figure 18(e)), 6) a second layer of Si$_3$N$_4$ with a thickness of 100 nm was deposited and patterned for passivation from the top side (Figure 18(f)). Optical images of the fabricated devices are shown in Figure 1d.

Experimental Set up and Details of the Microbolometer Voltage Noise PSD Study

The noise voltage power spectral density (PSD) of amorphous Si$_x$Ge$_y$O$_{1-x-y}$ based microbolometers were optimized and reduced by annealing the devices in vacuum at the temperature of 200 °C, 250 °C or 300 °C with a ramp rate of 10 °C/min for 1 to 5 hours of annealing duration. The noise measurements were performed on devices without air gaps with various Si-Ge-O compositions. Many devices from four wafers with different compositions of Si-Ge-O were measured before and after annealing at different bias currents. The noise measurements were performed in air inside a cryostat (DE 202 cold head), which was placed inside a shielding room in order to isolate the microbolometer from any external sources of noise. The output voltage was fed to a dynamic signal analyzer (HP 35670A) which measures noise-per-unit bandwidth, through a low noise preamplifier (Signal Recovery Model #5113). The preamplifier gain was set to 1000 to amplify noise voltage PSD from the device. Each device was voltage biased using Ni-Cd battery and 1 MΩ metal resistor connected in series with the device (See Figure 19(a)). The applied currents were ranged between 0.08-0.7 μA. The noise was recorded over the frequency ranges 1- 25 kHz. We report noise study between 1-800 Hz with 0.5 Hz bandwidth for 4 devices namely W01, W02, W03, W04, each from one wafer with different composition.

Resistivity and TCR as a function of temperature

We have selected four Si$_x$Ge$_y$O$_{1-x-y}$ compositions, which were selected from over 340 deposited and characterized films [40] for noise characterization. The film compositions and electrical properties of the fabricated four wafers are listed in Table 5. The TCR and the corresponding resistivity of devices from the four wafers were plotted as a function of temperature as shown in Figure 21. These figures includes
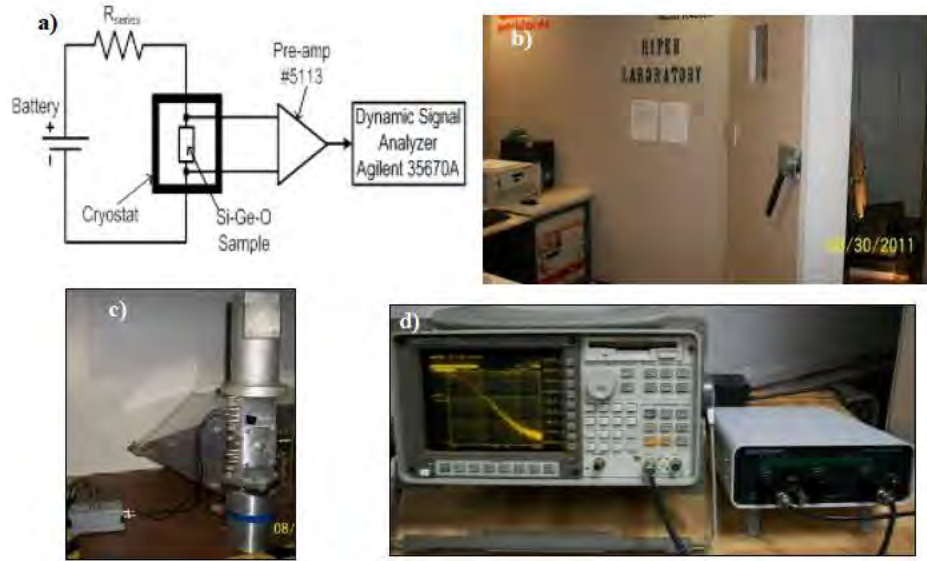
Figure 19. a) Schematic of noise measurement setup, **b)** Shielding room, **c)** Cryostat inside inside the shielding room, **d)** Dynamic signal analyzer and Preamplifier).

four films with a relatively high TCR along with low resistivity values measured at room temperature of – 3.518 %/K, and 763 Ω-cm, –2.590 %/K and 1.170 kΩ-cm, –3.864 %/K and 3.573 kΩ-cm, and –3.103 %/K, and 730 Ω-cm using $Si_{0.053}Ge_{0.875}O_{0.072}$, $Si_{0.041}Ge_{0.902}O_{0.057}$, $Si_{0.081}Ge_{0.853}O_{0.066}$ and $Si_{0.034}Ge_{0.899}O_{0.067}$ respectively. The TCR denoted by "Measured", was plotted from the measured data directly. The TCR denoted by "Calculated", was determined and plotted using Eq. 2, where the E_a was deduced from the slope of Arrhenius plot. It is noted that the R-T behavior of the $Si_xGe_yO_{1-x-y}$ films in the device were exponential and followed the relation in Eq. 2. At room temperature, wafer 02 showed the lowest value of TCR while the other three wafers have almost similar values of TCR at room temperature. However, the figure shows that TCR values around room temperature of wafer 03 (Figure 21) were not stable with large fluctuations which may have resulted in a higher 1/f-noise value. In addition, the devices did not work with a large number of biasing current since the resistivity is very high. The current-voltage (I-V) characteristics were measured before and after annealing the fabricated devices (Figure 20). It was found to be linear and the devices did not suffer Joule heating effect. The linear region of wafer 03 is -300 nA to 300 nA. After that there was no stable current voltage relationship for this wafer because wafer 3 the resistivity was very high. Wafer 01 is linear between -760 nA to 760 nA that is the maximum linear region than any other device and completely straight line.

Table 5: Film composition and electrical properties of the devices.

Wafer	Film Composition	Resistivity ($\times 10^3$ Ω-cm)	TCR (%/K)	Activation Energy E_a (eV)
W01	$Si_{0.053}Ge_{0.875}O_{0.072}$	0.763	–3.518	0.2656
W02	$Si_{0.041}Ge_{0.902}O_{0.057}$	1.170	–2.590	0.1956
W03	$Si_{0.081}Ge_{0.853}O_{0.066}$	3.573	–3.864	0.2917
W04	$Si_{0.034}Ge_{0.899}O_{0.067}$	0.730	–3.103	0.2402

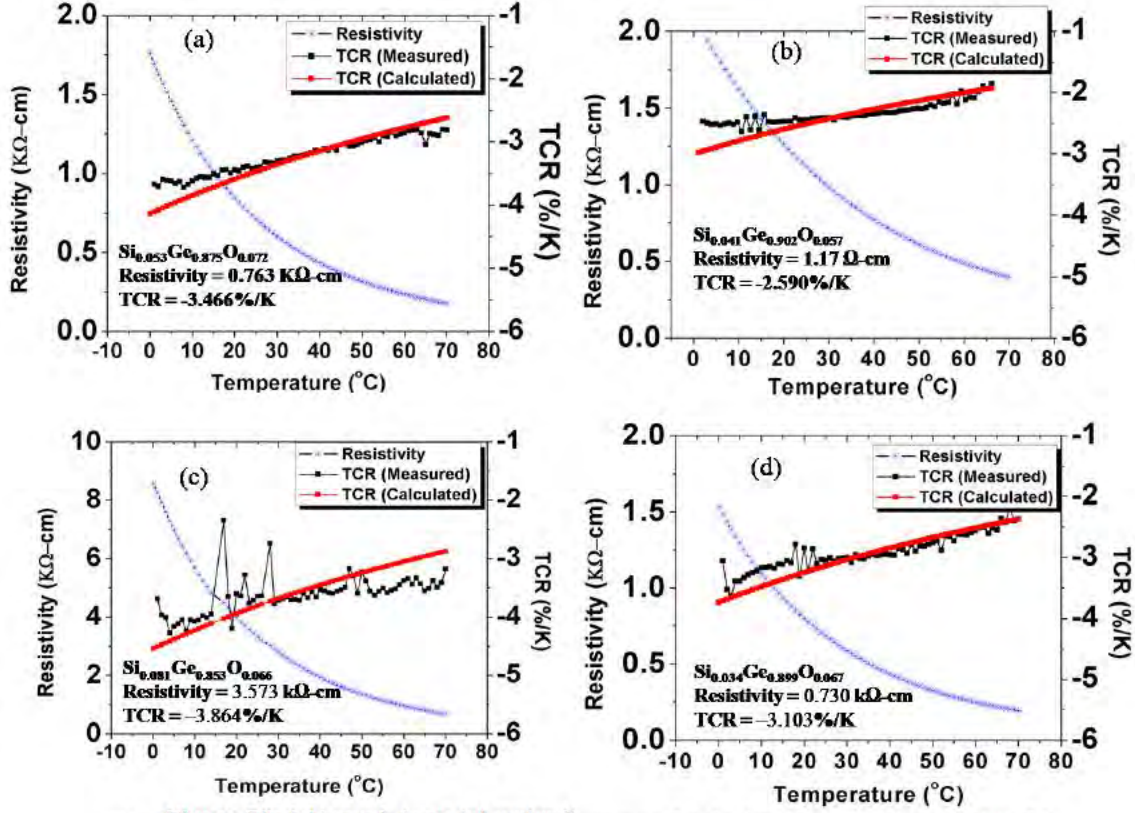Figure 20: I-V graph from (a) wafer W01, (b) W02, c) W03 and d) W04.

Figure 21: Resistivity and TCR versus temperature for devices from wafer (a) W01, (b) W02, c) W03 and d) W04.

Noise study of metal resistor

Each device was voltage biased using Ni-Cd battery and 1 MΩ load resistor connected in series with the device. The applied currents ranged between 0.08-0.6 µA. We have selected metal resistor because they have much lower $1/f$-noise than that of carbon resistors [72, 73]. The measured $1/f$-noise of 11.5 kΩ, 51 kΩ, and 1 MΩ metal resistors are shown in Figure 22. The $1/f$-noise corner frequencies were 6 Hz, 3 Hz and 2.5 Hz, respectively. The figure also shows how increasing the resistance increases PSD voltage noise without applying any biasing current or voltage, since Johnson noise is linearly dependent on resistance and excess fluctuation of electrons at room temperature.

Noise study of microbolometer before annealing

We have measured the voltage noise PSD of the fabricated wafers as a function of frequency at bias current between 0.07 – 0.6 µA before and after annealing. Figure 23 shows the noise spectrum of devices from wafer W01 (namely W01D21) and wafer W04 (namely W04D33) before annealing. The figure clearly demonstrates that the noise increases as the biasing current increases in all devices. The lowest measured noise voltage PSD of device W01D21 and W04D33 were 7.59×10^{-15} V^2/Hz, and 2.79×10^{-14} V^2/Hz at 25 Hz and 160 Hz, respectively. The corresponding Hooge's parameters γ, β and K_f were 1.19, 1.71, 3.65×10^{-14} and 1.58, 2.19, 2.74×10^{-13}, respectively. The Hooge's parameters and $1/f$ noise at the corner frequency for the four wafers are shown in Table 6. We see in the table that the average value of γ was close to 1, ranged between 0.91 - 1.26 for wafer W01 and W02. This indicates that the $1/f$-noise is dominant at low frequencies. But for the wafer W03 and W04 we found the γ is close to 2, indicating the presence of brown noise before annealing. Noise may have come from different part of the

45

device, and from several sources of noise, i.e. surface defects, dangling bond, etc. [70]. The presence of red noise in wafer W03 and W04 may have attributed by this coupling effect of more than one source of noise, i.e. surface defects, dangling bond, etc. Later we will show that annealing the devices in vacuum abridges this red noise effect, reinstating $1/f$ noise as the main contributor. The value of K_f for different devices from two Wafers (W01 and W04) before annealing was ranged from 3.65×10^{-14} to 6.02×10^{-10}. The lower values of this range demonstrates that some film compositions have a relatively lower voltage noise PSD. The results shows that the voltage noise PSD of the four wafers were different before annealing, with the lowest is observed in wafer W01 and the highest is in wafer W04. This indicates that the noise sources in the microbolometer are due to the presence of trapping states, detrapping of carriers, and defects in $Si_xGe_yO_{1-x-y}$ sensing layer. In this work, we will show that annealing the devices in vacuum will reduce the voltage noise PSD and eliminate the brown noise effect, and thus reinstating $1/f$ noise as the main contributor. The encapsulation of $Si_xGe_yO_{1-x-y}$ with two Si_3N_4 passivation layers might have played a dominant role in minimizing surface state effects in $Si_xGe_yO_{1-x-y}$ which in turn reduced $1/f$ noise [73]. This might have diminished the electron–hole recombination rate by lowering the density of interface traps and decreasing the dangling bond, and thus reducing the $1/f$ noise [74]. In addition, the passivation layers might have increased the mobility of the surface state in $Si_xGe_yO_{1-x-y}$ thin films, which can be a result of dislocations, and chemical residues [75, 76]. This will also lead to a lower $1/f$ noise. In addition, we have not observed any sudden increase in the noise level across the frequency spectrum in Figure 23. Thus, our devices do not suffer from generation – recombination (g-r) noise.

Noise study of microbolometer after annealing

Many devices from the same four wafers were annealed at 200 °C, 250 °C and 300 °C from 1 to 5 hours. Figure 24 shows the measured noise voltage PSD for 6 devices from wafer W04 and W01 before and after annealing at 200 °C, 250 °C, and 300 °C for duration from 1 hour to 5 hours using a bias current of 0.07 µA. The corresponding Hooge's parameters for the devices from same two wafers are presented in Table 7 and Table 8 respectively. The figure shows that the voltage noise PSD of the devices was decreased as the annealing time increased. For example, the lowest measured noise for the device (W04D33) that was annealed at 300 °C was 1.96×10^{-14} V^2/Hz at 12 Hz (before . After 4 hours of annealing was 2.79×10^{-14} at 160 Hz). The comparison between the noise voltage PSDs at the new corner frequency (12 Hz) with the corresponding noise level before annealing at the same frequency indicates a factor of 40 decrease in noise. After 4 hours of annealing, the voltage noise started to increase again. It is noted that annealing at higher temperature 300 °C reduced the low frequency voltage noise PSD more
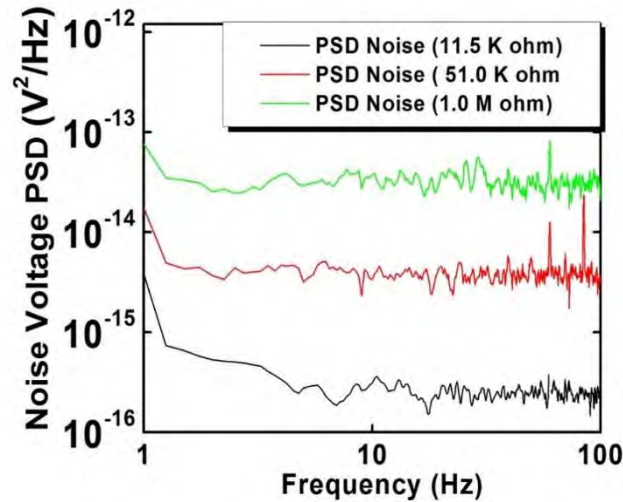

Figure 22: PSD noise comparison with different metal resistances:
11.5 KΩ, 51 KΩ and 1 MΩ without biasing current.

46

than that of 200 °C and 250 °C temperature. The average value of γ was close to 1, was 0.8 for device W04D33, after 4 hours of annealing at 300 °C. This results clearly indicates that annealing have reduced the effect of any other noise sources, making the 1/f- noise as the main contributing source. The corresponding 1/f-noise coefficient (K_f) of device W04D33 was changed from 2.74×10^{-13} to 1.84×10^{-14} after 4 hours of annealing at 300 °C. The K_f value started to increase after annealing at higher time interval. This increase is attributed to the reduction in 1/f-noise and the increase of β with increasing annealing time interval. In addition, the results show that annealing the devices has reduced the voltage noise PSD significantly on one wafer (wafer W04), and the 1/f-noise PSD was decreased significantly on devices that had abnormally high 1/f-noise before annealing (Figure 24c).

Table 6: Noise parameters of the devices before annealing for wafers W01 to W04.

Wafer	Device No.	Γ	β	K_f	Noise PSD (V^2/Hz) at corner freq
	W01D21	1.19	1.71	3.65×10^{-14}	7.59×10^{-15} at 025 Hz with 70 nA
W01	W01D22	1.26	2.24	1.44×10^{-12}	1.88×10^{-14} at 080 Hz with 70 nA
	W01D52	0.93	2.21	3.46×10^{-13}	3.56×10^{-14} at 030 Hz with 80 nA
W02	W02D45	0.91	1.93	3.01×10^{-14}	1.89×10^{-14} at 12 Hz with 85 nA
W03	W03D46	1.85	2.00	3.19×10^{-16}	3.24×10^{-14} at 70 Hz with 80 nA
	W04D43	1.78	2.62	3.33×10^{-11}	4.12×10^{-14} at 200 Hz with 80 nA
W04	W04D11	2.00	1.83	6.02×10^{-10}	5.58×10^{-13} at 200 Hz with 80 nA
	W04D33	1.58	2.19	2.74×10^{-13}	2.79×10^{-14} at 160 Hz with 90 nA

Annealing devices from wafer 01 have reduced the noise voltage PSD slightly. The lowest measured noise voltage PSD after annealing was on device W01D52, the noise and corner frequency was changed from 3.56×10^{-14} V^2/Hz at 030 Hz to 5×10^{-14} V^2/Hz at 10 Hz (Fig. 8f). The comparison between the voltage noise PSD at the new corner frequency (10 Hz) with the corresponding noise level before annealing at the same frequency indicates slight reduction in noise level. The corresponding 1/f-noise coefficient (K_f) of wafer W01 was changed from 3.46×10^{-13} to 1.44×10^{-13} after 4 hours of annealing at 300 °C. The small decrease in K_f value is due to the low 1/f-noise before annealing the devices. However, annealing at lower temperature did not reduce the voltage noise at all. In fact, the noise was increased significantly with increasing annealing time interval. It is important to note that annealing did help reducing the noise in devices that have abnormally high voltage noise before annealing. In this case, annealing helped reducing the noise but it stayed within the range of wafer W01 noise level before annealing (Figure 24d).

Table 7. Variation of Hooge's parameters in different devices with different annealing time intervals for wafer W04.

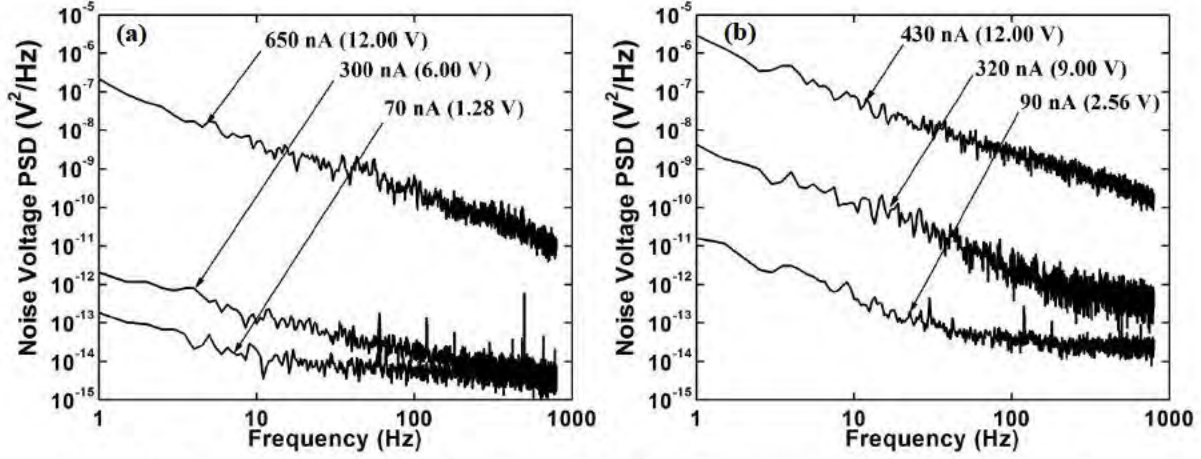| Annealing Duration (Hours)	W04D43 @ 200° C			W04D11 @ 250° C			W04D33 @ 300° C		
	γ	β	K_f	γ	β	K_f	γ	β	K_f
0	1.78	2.62	3.33×10^{-11}	2.00	1.83	6.02×10^{-10}	1.58	2.19	2.74×10^{-13}
1	1.87	1.82	2.30×10^{-11}	1.80	6.33	5.87×10^{-08}	0.95	1.43	1.81×10^{-13}
2	0.99	2.04	2.39×10^{-13}	0.82	2.51	2.42×10^{-13}	1.37	3.50	1.56×10^{-14}
3	1.22	2.41	4.16×10^{-13}	0.76	1.55	2.19×10^{-16}	0.81	2.56	1.36×10^{-14}
4	2.07	2.59	9.55×10^{-09}	1.06	3.92	7.17×10^{-15}	0.80	2.33	1.84×10^{-14}
5	1.83	0.20	6.77×10^{-08}	1.18	2.81	4.43×10^{-14}			

Figure 23: PSD noise with different biasing currents for before annealing: a) W01D21; b) W04D33.

Table 8: Variation of Hooge's parameters in different devices with different annealing time intervals for Wafer W01.

Annealing Duration (Hours)	W01D21 @ 200 °C			W01D22 @ 250 °C			W01D52 @ 300 °C		
	γ	β	K_f	γ	β	K_f	γ	β	K_f
0	1.19	1.71	3.65×10^{-14}	1.26	2.24	1.44×10^{-12}	0.93	2.21	3.46×10^{-13}
1	1.06	2.68	7.53×10^{-12}	1.60	1.73	8.49×10^{-11}	1.03	2.00	6.34×10^{-13}
2	1.13	1.94	9.74×10^{-11}	1.00	1.88	2.23×10^{-13}	1.01	2.38	5.00×10^{-13}
3	1.62	2.00	8.02×10^{-11}	1.02	1.99	3.90×10^{-13}	0.92	2.11	3.26×10^{-13}
4	1.48	1.70	1.27×10^{-10}	0.95	2.00	2.02×10^{-13}	0.86	2.30	1.44×10^{-13}
5	1.58	0.65	8.90×10^{-09}	0.88	3.82	1.96×10^{-14}			

The results show that three wafers have relatively similar noise level while wafer W04 has the highest voltage noise before annealing. As the annealing time interval of the devices increases, the electrical noise level was reduced. This indicates that annealing at a specific time interval reduced the trapping states or defects in around 160 Hz to around 12 Hz (W04D33) and to 10 Hz in (W01D52) which indicates that Johnson noise can be observed below 12 Hz, and 10 Hz, respectively. Below 12 Hz or 10 Hz, the frequency is dominated by $1/f$ noise. The other two wafers behaved similarly but with different noise level and different corner frequency.

We have plotted the lowest measured voltage noise PSD at 0.07 µA of the four wafers before and after annealing (Figure 25). The results show that three wafers (W01, W02, and W03) have relatively similar noise level while wafer W04 has the highest voltage noise before annealing. This might be due to the higher Ge concentration in the film.
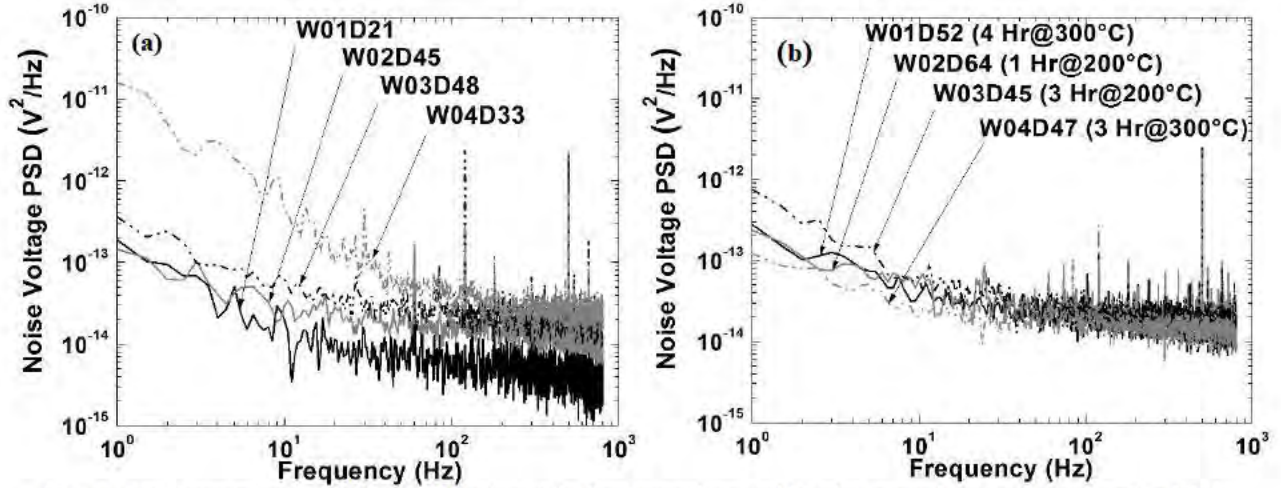
Figure 25: Comparison with low PSD noise: a) before annealing and b) after annealing from four wafers W01-W04 at biasing current of 80 nA.

Another potential source of $1/f$ noise is the bond formation of $Si_xGe_yO_{1-x-y}$ sensing layer in terms of Si-O and Ge-O bond formation [44, 45]. The bonds might have resulted in large number of defects in the film and thus contributed to the presence of $1/f$-noise. The bonding of Si with O creates paramagnetic defects which leads to unpair of electron with a silicon dangling bond [77]. Similarly, Ge-O and Ge-Ge bonding leads to dangling bond of Ge. The XRD study of the four wafers, confirmed the presence of Dangling bonds since we have not observed any sharp peak in the spectrum, suggesting amorphous nature of all films, and lack of long range order. In addition, to the presence of dangling bonds, the presence of deep traps and recombination centers in Si-Ge bond, and the interface between NiCr metal and $Si_xGe_yO_{1-x-y}$ semiconductor film might have contributed to the increase in $1/f$-noise level [78, 79]. The metal semiconductor interface might have contributed to the noise level due to the cleanliness of the contacts and the possible formation of Schottky junction [44]. After 4 hours annealing in vacuum at low pressure, we have observed significant reduction in noise in wafer W04, and slight reduction in the wafer W01.
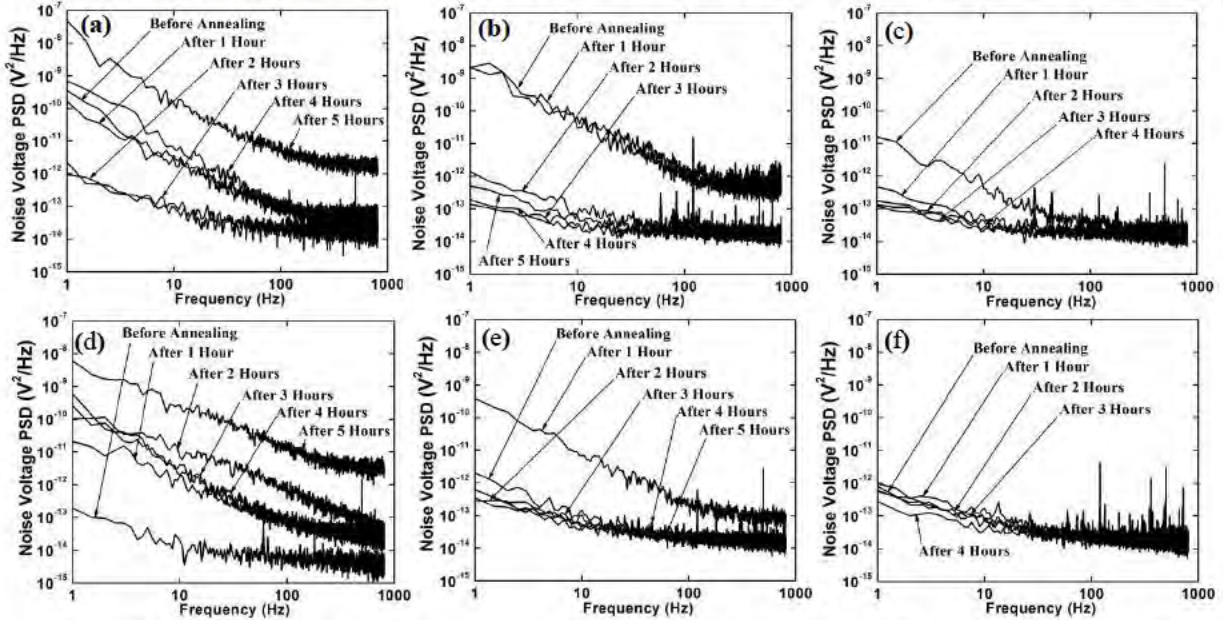

Figure 24: Noise PSD before and after annealing for different durations: in W04, devices a) W04D43, b) W04D11 and c) W04D33 annealed at 200 °C, 250 °C and 300 °C respectively; in W01, devices d) W01D21, e) W01D22, f) W01D52 annealed at 200 °C, 250 °C and 300 °C respectively

This indicates that annealing in vacuum has reduced the number of dangling bond, recombination centers, and impacted the metal-semiconductor interface. After 3-5 hours of annealing, the voltage noise PSD starts to increase significantly. This might be due to the increase of dangling bonds, low field mobility [76] and the oxide traps [80]. In addition, the long exposure to heat during annealing might have increased some source of $1/f$ noise such as the dislocations, surface and bulk phenomena [27, 37, 81, 82].

It is known that camera frame rate is 30 Hz and 60 Hz. So, it is very important to observe the low frequency noise at lower camera frame. Table 9 presents the noise voltage PSD for before and after annealing at 30 Hz. The noise voltage PSD was the highest for device W03D46 from wafer 03 before and after annealing at 30 Hz. The device W04D33 from wafer 04 demonstrated the lowest noise after annealing which reduced from 4.5×10^{-13} to 1.30×10^{-14} (V^2/Hz). However, all devices, in Table 6, show declining trend after annealing devices at 30 Hz.

Table 9. Comparison with Low PSD Noise before and after Annealing at 30 Hz- IR Thermal Camera Frame Rate

Wafer	Noise Voltage PSD Before Annealing (V^2/Hz)	Noise Voltage PSD After Annealing (V^2/Hz)
W01D52	3.89×10^{-14}	2.59×10^{-14}
W02D63	4.77×10^{-14}	2.33×10^{-14}
W03D46	8.1×10^{-14}	3.42×10^{-14}
W04D33	4.5×10^{-13}	1.30×10^{-14}

THESIS

1. Hai, Muhammad Lutful, PhD. ECE, (Expected to Graduate December 2014). Thesis: Uncooled Si$_x$Ge$_{1-x}$O$_{1-x-y}$ Infrared Sensitive Material and Uncooled infrared microbolometer.

7. Jalal, Md. E., MS. ECE, (Graduated May 2014). Thesis: Noise Optimization of Amorphous Si$_x$Ge$_y$O$_{1-x-y}$ Uncooled microbolometer.

REFERENCES

[1]   P. W. Norton and M. Kohin, "Technology and Application Advancements of Uncooled Imagers," *Proc. SPIE,* vol. 5783, pp. 524-530, 2005.
[2]   D. Murphy, M. Ray, A. Kennedy, J. Wyles, C. Hewitt, R. Wyles*, et al.*, "Expanded applications for high performance VOx microbolometer FPAs," *Proc. SPIE,* vol. 5783, p. 448, 2005.
[3]   C. M. Hanson, S. K. Ajmera, J. Brady, T. Fagan, W. McCardel, D. Morgan*, et al.*, "Small pixel a-Si/a-SiGe bolometer focal plane array technology at L-3 Communications," *Proc. SPIE,* vol. 7660, p. 76600R, 2010.
[4]   C. M. Hanson, H. R. Beratan, and D. L. Arbuthnot, "Uncooled thermal imaging with thin-film ferroelectric detectors," *Proc. SPIE,* vol. 6940, p. 694025, 2008.

[5]   C. M. Hanson, "Compact, Rugged, and intuitive thermal imaging cameras for homeland security and law enforcement applications," *Proc. SPIE,* vol. 5778, pp. 751-756, 2005.

[6]   T. Schimert, J. Brady, T. Fagan, M. Taylor, W. McCardel, R. Gooch*, et al.*, "Amorphous silicon based large-format uncooled FPA microbolometer technology," *Proc. SPIE,* vol. 6940, pp. 694023-1-7, 2008.

[7]   T. Schimert, C. Hanson, J. Brady, T. Fagan, M. Taylor, W. McCardel*, et al.*, "Advances in small-pixel, large-format *a*-Si bolometer arrays," *Proc. SPIE,* vol. 7298, p. 72980T, 2009.

[8]   S. K. Ajmera, A. J. Syllaios, G. S. Tyber, M. F. Taylor, and R. E. Hollingsworth, "Amorphous silicon thin-films for uncooled infrared microbolometer sensors," *Proc. SPIE,* vol. 7660, p. 766012, 2010.

[9]   S. Black, M. Ray, C. Hewitt, R. Wyles, E. Gordon, K. Almada*, et al.*, "RVS uncooled sensor development for tactical applications," *Proc. SPIE,* vol. 6940, p. 694022, 2008.

[10]   D. Murphy, M. Ray, J. Wyles, and e. al. , "640 × 512 17 μm Microbolometer FPA and sensor development," *Proc. SPIE,* vol. 6542, p. 65421Z, 2007.

[11]   S. J. Ropson, J. F. Brady III, G. L. Francisco, J. Gilstrap, R. W. Gooch, P. McCardel*, et al.*, "a-Si 160 × 120 Micro IR camera: operational performance," *Proc. SPIE,* vol. 4393, pp. 89-98, 2001.

[12]   C. Li, C. J. Han, G. D. Skidmore, and C. Hess, "DRS uncooled VOx infrared detector development and production status," *Proc. SPIE,* vol. 7660, p. 76600V, 2010.

[13]   C. Li, G. Skidmore, C. Howard, E. Clarke, and C. J. Han, "Advancement in 17-micron pixel pitch uncooled focal plane arrays," *Proc. SPIE,* vol. 7298, p. 72980S, 2009.

[14]   C. J. Han, C. G. Howard, P. E. Howard, A. C. Ionescu, C. C. Li, J. C. Monson*, et al.*, "Progress in DRS production line for uncooled focal plane arrays," *Proc. SPIE,* vol. 5406, pp. 483-490, 2004.

[15]   P. E. Howard, J. E. Clarke, A. C. Ionescu, C. Li, and A. Frankenberger, "Advances in uncooled 1-mil pixel size focal plane products at DRS," *Proc. SPIE,* vol. 5406, pp. 512-520, 2004.

[16]   R. Blackwell, G. Franks, D. Lacroix, S. Hyland, and R. Murphy, "Small pixel uncooled imaging FPAs and applications," *Proc. SPIE,* vol. 7660, p. 76600Y, 2010.

[17]   R. Blackwell, D. Lacroix, T. Bach, J. Ishii, S. Hyland, T. Dumas*, et al.*, "17 μm microbolometer FPA technology at BAE Systems," *Proc. SPIE,* vol. 7298, p. 72980P, 2009.

[18]   R. Blackwell, D. Lacroix, T. Bach, J. Ishii, S. Hyland, J. Geneczko*, et al.*, "Uncooled VOx thermal imaging systems at BAE Systems," *Proc. SPIE,* vol. 6940, p. 694021, 2008.

[19]   R. J. Blackwell, T. Bach, D. O'Donnell, J. Geneczko, and M. Joswick, "17 μm pixel 640 × 480 microbolometer FPA development at BAE systems," *Proc. SPIE,* vol. 6542, p. 65421U, 2007.

[20]   R. Murphy, M. Kohin, B. S. Backer, N. R. Butler, R. J. Blackwell, and T. Allen, "Recent developments in uncooled IR technology," *Proc. SPIE,* vol. 4028, pp. 12-16, 2000.

[21]   P. W. Kruse, R. Dodson, S. Anderson, L. Kantor, M. Knipfer, T. J. McManus*, et al.*, "Infrared imager employing a 160 × 120 pixel uncooled bolometer array," *Proc. SPIE,* vol. 3436, pp. 572-577, 1998.

[22]   J. L. Tissot, A. Durand, T. Garret, C. Minassian, P. Robert, S. Tinnes*, et al.*, "High performance uncooled amorphous silicon VGA IRFPA with 17μm pixel-pitch," *Proc. SPIE,* vol. 7660, p. Tissot_VGA_2010, 2010.

[23]   J. J. Yon, J. P. Nieto, L. Vandroux, P. Imperinetti, E. Rolland, V. Goudon*, et al.*, "Low-resistance a-SiGe-based microbolometer pixel for future smart IR FPA," *Proc. SPIE,* vol. 7660, p. 76600U, 2010.

[24]   A. Durand, C. Minassian, J. L. Tissot, M. Vilain, P. Robert, A. Touvignon*, et al.*, "Uncooled amorphous silicon TEC-less 1/4 VGA IRFPA with 25 μm pixel-pitch for high volume applications," *Proc. SPIE,* vol. 7298, p. 72982B, 2009.

[25]   A. Trouilleau, B. Fièque, S. Noblet, F. Giner, D. Pochic, A. Durand*, et al.*, "High-performance uncooled amorphous silicon TEC less XGA IRFPA with 17 μm pixel-pitch," *Proc. SPIE,* vol. 7298, p. 72980Q, 2009.

[26]   J. J. Yon, E. Mottin, and J. L. Tissot, "Latest amorphous silicon microbolometer developments at LETI-LIR," *Proc. SPIE,* vol. 6940, p. 69401W, 2008.

[27]   J. J. Yon, A. Astier, S. Bisotto, G. Chamingis, A. Durand, J. L. Martin*, et al.*, "First demonstration of 25 μm pitch uncooled amorphous Silicon microbolometer IRFPA at LETI-LIR," *Proc. SPIE,* vol. 5783, pp. 432-440, 2005.

[28]   B. Fièque, J. L. Tissot, C. Trouilleau, A. Crastes, and O. Legras, "Uncooled microbolometer detector: recent development at ULIS," *Infrared Physics & Technology,* vol. 49, pp. 187-191, 2007.

[29]   F. Williamson, L. Marchese, G. Baldenberger, F. Ch\^ateauneuf, F. Provencal, J.-S. Caron*, et al.*, "Advanced microbolometer detectors for a next-generation uncooled FPA for space-based thermal remote sensing," *Proc. SPIE,* vol. 7208, p. 72080J, 2009.

[30] T. Pope, F. Dupont, S. G. Blanco, F. Williamson, C. Chevalier, L. Marchese, *et al.*, "Space qualification of a 512×3 pixel uncooled microbolometer FPA," *Proc. SPIE,* vol. 7298, p. 729826, 2009.

[31] K. A. Hay, "Uncooled focal plane array detector development at infrared vision technology corporation," *Proc. SPIE,* vol. 5783, pp. 514-523, 2005.

[32] K. A. Hay, "Large format VOx microbolometer UFPA development at ITC," *Proc. SPIE,* vol. 6295, p. 629505, 2006.

[33] U. Mizrahi, L. Bikov, A. Giladi, N. Shiloah, S. Elkind, T. Czyzewski, *et al.*, "New developments in SCD's 17-μm VOx μ-bolometer product line," *Proc. SPIE,* vol. 7660, p. 76600W, 2010.

[34] C. Li, C. J. Han, and G. Skidmore, "Overview of DRS uncooled VOx infrared detector development," *Optical Engineering,* vol. 50, pp. 061017-061017, 2011.

[35] J. E. Gray, Z. Celik-Butler, D. P. Butler, and M. F. Almasri, "Semiconducting YBaCuO as infrared-detecting bolometers," *Proc. SPIE,* vol. 3436, pp. 555-565, 1998.

[36] M. Almasri, D. P. Butler, and Z. Çelik-Butler, "Semiconducting YBCO bolometers for uncooled IR detection," *Proc. SPIE,* vol. 4028, pp. 17-26, 2000.

[37] M. Almasri, D. P. Butler, and Z. Çelik-Butler, "Self-supporting uncooled infrared microbolometers with low-thermal mass," *Microelectromechanical Systems, Journal of,* vol. 10, pp. 469-476, sep 2001.

[38] M. García, R. Ambrosio, A. Torres, and A. Kosarev, "IR bolometers based on amorphous silicon germanium alloys," *Journal of Non-Crystalline Solids,* vol. 338-340, pp. 744-748, 2004.

[39] M. L. Hai, M. Hesan, J. Lin, Q. Cheng, M. Jalal, A. J. Syllaios, *et al.*, "Uncooled silicon germanium oxide $(Si_xGe_yO_{1-x-y})$ thin films for infrared detection," *Proc. SPIE,* vol. 8353, p. 835317, 2012.

[40] R. Anvari, Q. Cheng, M. L. Hai, T. P. Bui, A. J. Syllaios, S. K. Ajmera, *et al.*, "Silicon germanium oxide $(Si_xGe_yO_{1-x-y})$ infrared sensitive material for uncooled detectors," *MRS Proceedings,* vol. 1245, pp. A18-04, 2010.

[41] Q. Cheng and M. Almasri, "Silicon Germanium Oxide $(Si_xGe_{1-x}O_y)$ infrared material for uncooled infrared detection," *Proc. SPIE,* vol. 7298, p. 72980K, 2009.

[42] A. H. Z. Ahmed, R. N. Tait, T. B. Oogarah, H. C. Liu, M. W. Denhoff, G. I. Sproule, *et al.*, "A Surface micromachined amorphous $Ge_xSi_{1-x}O_y$ bolometer for thermal imaging applications," *Proc. SPIE,* vol. 5578, pp. 298-308, 2004.

[43] M. M. Rana and D. P. Butler, "Amorphous Ge_xSi_{1-x} and $Ge_xSi_{1-x}O_y$ thin films for uncooled microbolometers," *Proc. SPIE,* vol. 5783, pp. 597-606, 2005.

[44] A. H. Z. Ahmed and R. N. Tait, "Characterization of amorphous $Ge_xSi_{1-x}O_y$ for micromachined uncooled bolometer applications," *J. appl. Phys.,* vol. 94(8), pp. 5326-5332, 2003.

[45] M. Clement, E. Iborra, J. Sangrador, and I. Barberan, "Amorphous $Ge_xSi_{1-x}O_y$ sputtered thin films for integrated sensor applications," *J. Vac. Sci. Technol.,* vol. 19(1), pp. 294-298, 2001.

[46] M. M. Rana and D. P. Butler, "Radio frequency sputtered $Si_{1-x}Ge_x$ and $Si_{1-x}Ge_xO_y$ thin films for uncooled infrared detectors," *Thin Solid Films,* vol. 514, pp. 355-360, 2006.

[47] M. V. S. Ramakrishna, G. Karunasiri, U. Sridhar, and G. Chen, "Performance of titanium and amorphous germanium microbolometer infrared detectors," *Proc. SPIE,* vol. 3666, pp. 415-420, 1999.

[48] J. S. Shie, Y. M. Chen, M. O. Yang, and B. C. S. Chou, "Characterization and modeling of metal-film microbolometer," *IEEE/ JMEMS,* vol. 5(4), pp. 298-306, 1996.

[49] S. Sedky, P. Fiorini, K. Baert, L. Hermans, and R. Mertens, "Characterization and optimization of infrared poly SiGe bolometers," *IEEE Transaction on Electron Devices,* vol. 46(4), pp. 675-682, 1999.

[50] S. Sedky, P. Fiorini, M. Caymax, C. Baert, L. Hermans, and R. Mertens, "Characterization of bolometers based on polycrystalline silicon germanium alloys," *Electron Device Letters, IEEE,* vol. 19, pp. 376-378, 1998.

[51] P. D. Moor, Y. Creten, C. Goessens, B. Grietens, V. Leonov, J. Vermeiren, *et al.*, "Thermal infrared detection using linear arrays of poly SiGe uncooled microbolometers," *15th ICM 2003,* pp. 140-142, 2003.

[52] W. A. Radford, R. Wyles, J. Wyles, J. B. Varesi, M. Ray, D. F. Murphy, *et al.*, "Microbolometer uncooled infrared camera with 20-mK NETD," *Proc. SPIE,* vol. 3436, pp. 636-645, 1998.

[53] C. A. Marshall, N. R. Butler, R. J. Blackwell, R. Murphy, and T. B. Breen, "Uncooled infrared sensors with digital focal plane array," *Proc. SPIE,* vol. 1746, pp. 23-31, 1996.

[54] D. Murphy, M. Ray, J. Wyles, J. Asbrock, C. Hewitt, R. Wyles, *et al.*, "Performance improvements for VOx microbolometer FPAs," *Proc. SPIE,* vol. 5406, pp. 531-540, 2004.

[55] C. M. Hanson and H. R. Beratan, "Thin film ferroelectrics: breakthrough," *Proc. SPIE,* vol. 4721, pp. 91-98, 2002.

[56] T. A. Enukova, N. L. Ivanova, Y. V. Kulikov, V. G. Marlyarov, and I. A. Khrebtov, "Amorphous silicon and germanium films for uncooled microbolometers," *Technical Physics Letter,* vol. 23, pp. 504-506, 1997.

[57] P. W. Kruse, "Principles of uncooled infrared focal plane arrays," in *Uncooled Infrared Imaging Arrays and Systems*. vol. 47, P. W. Kruse, D. D. Skatrud, R. K. Willardson, and E. R. Weber, Eds., ed New York: Academic Press, 1997, pp. 17-42.

[58] J. F. Brady III, T. R. Schimert, D. D. Ratcliff, R. W. Gooch, B. Ritchey, P. McCardel, *et al.*, "Advances in amorphous silicon uncooled IR systems," *Proc. SPIE,* vol. 3698, pp. 161-167, 1999.

[59] C. Vedel, J.-L. Martin, J.-L. Ouvrier-Buffet, J.-L. Tissot, M. Vilain, and J.-J. Yon, "Amorphous-silicon-based uncooled microbolometer IRFPA," *Proc. SPIE,* vol. 3698, pp. 276-283, 1999.

[60] M. Ruß, J. Bauer, and H. Vogt, "The geometric design of microbolometer elements for uncooled focal plane arrays," *Proc. SPIE,* vol. 6542, p. 654223, 2007.

[61] V. N. Leonov, Y. Creten, P. D. Moor, B. D. Bois, C. Goessens, B. Grietens, *et al.*, "Small two-dimensional and linear arrays of polycrystalline SiGe microbolometers at IMEC-XenICs," *Proc. SPIE,* vol. 5074, pp. 446-457, 2003.

[62] Q. Cheng, S. Paradis, T. Bui, and M. Almasri, "Design of Dual-Band Uncooled Infrared Microbolometer," *IEEE Sensors Journal,* vol. 11(1), pp. 167-175, 2011.

[63] X. He, G. Karunasiri, T. Mei, W. Zeng, J. P. Neuzil, and U. Sridhar, "Performance of microbolometer focal plane array under varying pressure," *IEEE electron Device Letters,* vol. 21, pp. 233-235, 2000.

[64] P. Eriksson, J. Y. Andersson, and G. Stemme, "Thermal characterization of surface-micromachined silicon nitride membranes for thermal infrared detectors," *IEEE/ JMEMS,* vol. 6, pp. 55-61, 1997.

[65] M. S. Liu, J. S. Haviland, and C. J. Yue, "Integrated infrared sensitive bolometers," 5260225, 1992.

[66] M. M. Rana and D. P. Butler, "Noise reduction of a-Si$_{1-x}$Ge$_x$Si$_y$ microbolometers by forming gas passivation," *Thin Solid Films,* vol. 516, pp. 6499-6503, 2008.

[67] E. L. Dereniak and G. D. Boreman, *Infrared detectors and systems*. New York: Wiley, 1996.

[68] M. Almasri, "Micromachined Semiconducting YBaCuO IR and FIR Detectors," PhD Dissertation, Electrical Engineering, Southern Methodist University, Dallas, Texas, 2001.

[69] M. Galeazzi, K. R. Boyce, R. Brekosky, J. D. Gygax, R. L. Kelley, D. Liu, *et al.*, "Non-ideal effects in doped semiconductor thermistors," *Low Temperature Detectors,* vol. 605, pp. 83-86, 2002.

[70] F. N. Hooge, "1/f noise sources," *Electron Devices, IEEE Transactions on,* vol. 41, pp. 1926-1935, 1994.

[71] P. J. Fish, *Electronic noise and low noise design*. New York: McGraw-Hill, Inc., 1993.

[72] T. Williams and J. Thomas, "A Comparison of the Noise and Voltage Coefficients of Precision Metal Film and Carbon Film Resistors," *Component Parts, IRE Transactions on,* vol. 6, pp. 58-62, 1959.

[73] H. J. Son, I. W. Kwon, and H. C. Lee, "Passivation Effect for the Reduction of 1/ f Noise in Poly(3,4-ethylenedioxythiophene):Poly(styrene sulfonate) Thin Films Based on Uncooled Type Microbolometer Applications," *Applied Physics Express,* vol. 2, p. 041501, 2009.

[74] A. Van der Ziel, *Noise in Solid State Devices and Circuits*, 1 ed.: Wiley-Interscience, 1986.

[75] A. G. Aberle, *Crystalline silicon solar cells : advanced surface passivation and analysis / Armin G. Aberle*. Sydney :: Centre for Photovoltaic Engineering, University of New South Wales, 1999.

[76] W. Guo, G. Nicholas, B. Kaczer, R. M. Todi, B. De Jaeger, C. Claeys, *et al.*, "Low-Frequency Noise Assessment of Silicon Passivated Ge pMOSFETs With TiN/TaN/ HfO$_2$ Gate Stack," *Electron Device Letters, IEEE,* vol. 28, pp. 288-291, 2007.

[77] S. Mukhopadhyay, P. V. Sushko, A. M. Stoneham, and A. L. Shluger, "Correlation between the atomic structure, formation energies, and optical absorption of neutral oxygen vacancies in amorphous silica," *Physical Review B,* vol. 71, p. 235204, 06/13/ 2005.

[78] T. Uchino, M. Takahashi, and T. Yoko, "Model of a switching oxide trap in amorphous silicon dioxide," *Physical Review B,* vol. 64, p. 081310, 08/08/ 2001.

[79] R. Hakimi and M. C. Amann, "Reduction of 1/f carrier noise in InGaAsP/InP heterostructures by sulphur passivation of facets," *Semiconductor Science and Technology,* vol. 12, p. 778, 1997.

[80] A. L. McWhorter, "1/f noise and germanium surface properties," in *Semiconductor Surface Physics*, R. H. Kingston, Ed., ed: University of Pennsylvania Press, Philadelphia, 1957, pp. 207-228.

[81] H. C. Montgomery, "Electrical Noise in Semiconductors," *Bell System Technical Journal,* vol. 31, pp. 950-975, 1952.

[82] L. Bess, "A Possible Mechanism for 1/f Noise Generation in Semiconductor Filaments," *Physical Review,* vol. 91, pp. 1569-1569, 09/15/ 1953.